P-ISSN 0126-3188
E-ISSN 2443-3926

BRIN
BADAN RISET
DAN INOVASI NASIONAL

METALURGI

VOLUME 38 No 2 2023

SCIENTIFIC JOURNAL ACCREDITATION NO.3/E/KPT/2019

National Research and Innovation Agency

METALURGI

VOLUME 38 NUMBER 2 2023

P-ISSN 0126-3188
E-ISSN 2443-3926

ACCREDITATION : SK No. 3/E/KPT/2019

Publisher :
National Research and Innovation Agency (BRIN)
B.J. Habibie Sains and Technology Area, Banten, Indonesia 15314

E-mail: metalurgi@brin.go.id

Science and technology journal, regularly published every year; one volume consists of 3 editions

PREFACE

The author gives thanks to Allah for bestowing His blessing and direction, allowing the **Metalurgi Journal Volume 38, Edition 2**, **2023** to be successfully published.

The first article results from Safitry Ramandhany and colleagues research activities on *Synthesis of NiCrAlx Microparticles using Dry Milling and Wet Milling Processes*. Lia Aryani and colleagues presented the second article, *The Effect of Bakelite Binders on Magnetic Properties and Hardness Values of MQP-Type Bonded NdFeB Magnets*. Miftakhur Rohmah and colleagues showed *The Effect of Hot Rolling and Solution Treatment on the Microstructure and Mechanical Properties of Fe-Mn-Si-Cr-Ni Shape Memory Alloy* in the following article. For the fourth article, Yeni Muriani Zulaida and colleagues discussed *The Effect of Al_2O_3 and Strring Time on Density and Porosity of Aluminum ADC 12 Foam*. The fifth article by Toni Bambang Romijarso and his colleagues discussed *The Influence of Cooling Variations on Mechanical and Microstructural Properties in the Manufacture of Dual Phase Steel by Annealing Intercritical Process.*

The publication of this volume in Metalurgi Journal will benefit the advancement of research in Indonesia.

EDITORIAL

METALURGI

ISSN 0126 – 3188 Vol. 38 No. 2, 2023

Keywords sourced from articles. This abstract is reproduced without permission or fee.

UDC (OXDCF) 621.74

Safitry Ramandhany[a,b], Djoko Triyono [a], Eni Sugiarti[b], Resetiana Dwi Desiati[b], Risma Yulita Sundawa[b] ([a] Department of Physics, University of Indonesia, [b] Research Center for Advanced Materials, National Research and Innovation Agency)

Metalurgi, Vol. 38 No. 2, 2023

Synthesis of NiCrAlx Microparticles using Dry Milling and Wet Milling Processes

The characteristics of synthesized NiCrAlY and NiCrAlZr composite powders produced by the milling process were investigated to understand the particle size, the shape of particles, and the properties of crystalline structure. The milling process was carried out by combining dry milling with the wet milling method to prevent agglomeration, produce a homogeneous alloy powder, and reduce the particle size. Ethanol was used during the wet milling process as a process control agent. The PSA (particle size analysis) showed that the particle size was effectively reduced from ±70 µm to less than 30 µm. In addition, surface structure analysis characterized by SEM (scanning electron microscope) revealed that particle shape changed from blocky particles after dry milling into flaky, flattened, and fragmented particles after wet milling. An XRD (x-ray diffraction) was used to identify the phases of powders before and after the mechanical milling process. Crystal structure analysis was calculated from the change of peak broadening in XRD peak spectra. The Williamson-hall method has been performed to calculate the strain and crystallite size of synthesized NiCrAlY and NiCrAlZr composite powder in the present study. The findings in this study show the characteristics of powders, which are important information for producing coatings with good performance.

Keywords: Dry milling, wet milling, particle size, crystallite size, NiCrAlY, NiCrAlZr

METALURGI

ISSN 0126 – 3188 Vol. 38 No. 2, 2023

Keywords sourced from articles. This abstract is reproduced without permission or fee.

UDC (OXDCF) 621.3678

Lia Aryani[a], Bintang Surya Bhakti[a], Ahmad Riziq Mubarok[a], Ardita Septiyani[b], Henny Mulyani[a], Nanang Sudrajat[b], Dedi[a,b,] ([a]Metallurgical Engineering, Jenderal Achmad Yani University, [b]Research Center for Advanced Materials, National Research and Innovation Agency)

Metalurgi, Vol. 38 No. 2, 2023

The Effect of Bakelite Binders on Magnetic Properties and Hardness Values of MQP-Type Bonded NdFeB Magnets

Permanent magnets are important in modern society as components in various devices used by many industries and consumers, especially in generators and electric motors. Bonded magnet technology allows combining powdered magnetic materials with polymers as a binder to produce magnetic components that can be applied to certain applications, such as SynRM (synchronous reluctance) motors. Bonded magnets are easy to form without sacrificing their magnetic properties, which are too large, and also reduce costs, making them more effective and efficient. This paper reports the results of a study on the manufacture of bonded magnets NdFeB using bakelite binder on MQP-type NdFeB magnets with a bakelite variation of 0.5 - 2 wt.%. The characterization included testing magnetic properties with Permagraph, morphology with SEM (scanning electron microscope), and hardness values with micro Vickers hardness tester. The results of this study obtained remanence values in the range 5.53 - 6.44 kG and hardness values in the range 341.8 - 507.9 HV for NdFeB bonded magnets. According to SEM observations, the bakelite polymer matrix has successfully bound NdFeB grains, and no porosity is visible.

Keywords: Magnet, bonded, NdFeB, bakelite

METALURGI

ISSN 0126 – 3188 Vol. 38 No. 2, 2023

Keywords sourced from articles. This abstract is reproduced without permission or fee.

UDC (OXDCF) 669.1

Miftakhur Rohmah[a], Emmanoela Carissa Sendouw[b], Rifqi Aulia Tanjung[b], Dedi Pria Utama[a], Efendi Mabruri[a] ([a]Research Center for Metallurgy, National Research and Innovation Agency, [b]Department of Materials and Metallurgical Engineering, Kalimantan Institute of Technology)

Metalurgi, Vol. 38 No. 2, 2023

Effect of Hot Rolling and Solution Treatment on the Microstructure and Mechanical Properties of Fe-Mn-Si-Cr-Ni Shape Memory Alloy

Fe-14Mn-4Si-8Ni-11Cr SMA (shape memory alloy) was designed as a smart material because of its specific properties, which can memorize the original shape, so it has the potential to dampen vibration in seismic structures. Memory effect is triggered by SIM (stress-induced martensitic) transformation from γ-austenite to ε-martensite (hexagonal close-packed / HCP) structure, and it is recovered by heating after unloading. This study investigated the effect of hot rolling and solution treatment on the microstructure and its relationship with hardness and SME (shape memory effect) properties. The as cast of Fe-14Mn-4Si-8Ni-11Cr was hot rolled (900 and 1000 °C) and solution treated (1000 and 1100 °C). After the thermomechanical process, all microstructures consist of γ-FCC (face-centered cubic), the annealing twins, and a fine band of ε-martensite. The grain size of the γ-phase is 29.43, 41.96, 42.44, and 45.57 μm for samples B, C, D, and E, respectively. The higher the temperature of hot rolling and solution treatment applied, the larger the grain size obtained, indirectly reducing the hardness to 299.93 BHN and 286.52 BHN for samples D and E. The coarsened austenite grain, a lower number of annealing twins, and the pre-existing line band of ε-martensite are favorable to obtain the enormous recovery strain, up to 8.26% for sample E.

Keywords: Fe-Mn-Si-Ni-Cr, SMA (shape memory alloy), SME (shape memory effect), strain recovery

METALURGI

ISSN 0126 – 3188 Vol. 38 No. 2, 2023

Keywords sourced from articles. This abstract is reproduced without permission or fee.

UDC (OXDCF) 669.721.5

Yeni Muriani Zulaida, Muhammad Nurul Izzudin, Suryana (Department of Metallurgy, Sultan Ageng Tirtayasa University)

Metalurgi, Vol. 38 No. 2, 2023

The Effect of Al_2O_3 and Stirring Time on Density and Porosity of Aluminum ADC 12 Foam

The instability of the foam forming during metallic foam manufacture commonly occurs, which will cause undesirable pores. The stability of the foam structure is one of the important factors. A stabilizer can maintain the foam cell during the melting process. In this study, the metal used is ADC12 with a 12 wt.% of Si element content, and the foaming agent is $CaCO_3$. $CaCO_3$ will produce gas to form bubbles in the melt during the solidification process and use a stabilizer to strengthen cell walls so that foam does not easily fall off or collapse. The stabilizer uses Al_2O_3 with the variation of Al_2O_3 are 1 to 3 wt.%. The stirring time is as variable as well. A stirring process is conducted to distribute foaming agents so that the foam distribution is more homogeny throughout the aluminum foam. The variation of the stirring time is carried out for 60, 120, and 180 seconds. The results show that as the time of stirring and the addition of stabilizer increases, the porosity will rise, but the density decrease. Compressive strength results show it has no significant relation with increasing the stabilizer and stirring time. The highest compressive strength is obtained in the sample with a stirring time of 120 seconds with an Al_2O_3 content of 1wt.%.

Keywords: Metal foam, foaming agent, stirring, Al_2O_3

METALURGI

ISSN 0126 – 3188 Vol. 38 No. 2, 2023

Keywords sourced from articles. This abstract is reproduced without permission or fee.

UDC (OXDCF) 669.14

Toni Bambang Romijarso[a,b], Miftakhur Rohmah[a], Myrna Ariati[b], Efendi Mabruri[a], and Eddy Sumarno Siradj[b] ([a]Research Center for Metallurgy, National Reasearch and Innovation Agency, [b]Department of Metallurgy and Materials Engineering, Universitas Indonesia)

Metalurgi, Vol. 38 No. 2, 2023

The Influence of Cooling Variations on Mechanical and Microstructural Properties in the Manufacture of Dual Phase Steel by Annealing Intercritical Process

The present research focused on determining the effect of cooling-medium-induced initial structure before the intercritical annealing induced dual-phase structure in the low alloy steel. Low carbon steel, which consists of containing 0.09 wt.% C was heated at 920 °C for 30 minutes to austenitization and then cooled in various media to provide the different initial structures before the IA (intercritical annealing) process. After austenization, the cooling process in the furnace and open-air provided a ferrite-pearlite phase, while the cooling process in water generated full martensite as the initial structure. Afterwards, the sample was intercritical-annealed at 750 °C (temperature between Ac1 and Ac3 lines or intercritical zone) for 10 minutes and then quenched in water. The water quenching after the austenitizing process improved the mechanical strength of steel (919 MPa), compared to the as-received state (519 MPa) due to martensite formation. As the cooling rate increased after the austenitizing process, the tensile strength increased and the elongation decreased. The different structures before intercritical annealing affected the martensite volume fraction and further correlated with improving mechanical properties. The ferrite and pearlite, as the initial structure before the IA process, provide a smaller fraction of martensite (18.36 vol.% for furnace cooling and 27.85 vol.% for open-air cooling). In contrast, the full martensite as the initial structure before IA generates a higher fraction of martensite (39.25 vol.%). The tensile strengths obtained were 512, 516, and 541 MPa with elongations of 29.8%, 30.1% and 32.6% for cooling furnace, open air and water, respectively. The strain-hardening behavior during the intercritical annealing is not affected by the initial process of the structure.

Keywords: Dual-phase steel, intercritical anealing, low-alloy carbon steel, fraction of martensite

Metalurgi (2023) 2: 41 - 48

METALURGI
Majalah Ilmu dan Teknologi
p-ISSN 0126-3188 | e-ISSN 2443-3926
ejurnalmaterialmetalurgi.lipi.go.id

SYNTHESIS OF NiCrAlX MICROPARTICLES USING DRY MILLING AND WET MILLING PROCESSES

Safitry Ramandhany[a,b], Djoko Triyono [a*], Eni Sugiarti[b], Resetiana Dwi Desiati[b], Risma Yulita Sundawa[b]

[a] Department of Physics, University of Indonesia
Kampus UI, Kukusan, Depok, Indonesia 16424
[b] Research Center for Advanced Materials, National Research and Innovation Agency
B.J. Habibie Sains and Technology Area, Banten, Indonesia 15314
*E-mail: djoko.triyono@sci.ui.ac.id

Received: 15-05-2023, Revised: 30-06-2023, Accepted: 15-07-2023

Abstract

The characteristics of synthesized NiCrAlY and NiCrAlZr composite powders produced by the milling process were investigated to understand the particle size, the shape of particles, and the properties of crystalline structure. The milling process was carried out by combining dry milling with the wet milling method to prevent agglomeration, produce a homogeneous alloy powder, and reduce the particle size. Ethanol was used during the wet milling process as a process control agent. The PSA (particle size analysis) showed that the particle size was effectively reduced from ±70 µm to less than 30 µm. In addition, surface structure analysis characterized by SEM (scanning electron microscope) revealed that particle shape changed from blocky particles after dry milling into flaky, flattened, and fragmented particles after wet milling. An XRD (x-ray diffraction) was used to identify the phases of powders before and after the mechanical milling process. Crystal structure analysis was calculated from the change of peak broadening in XRD peak spectra. The Williamson-hall method has been performed to calculate the strain and crystallite size of synthesized NiCrAlY and NiCrAlZr composite powder in the present study. The findings in this study show the characteristics of powders, which are important information for producing coatings with good performance.

Keywords: *Dry milling, wet milling, particle size, crystallite size, NiCrAlY, NiCrAlZr*

1. INTRODUCTION

NiCrAlX (X: minor elements, i.e., Y, Zr, Hf, Ti, Si) alloys are used in TBC (thermal barrier coating) systems, which provide turbine blades with protection against oxidation and corrosion at high temperatures [1]-[3]. A critical factor against high-temperature oxidation is the performance of protective oxide on the turbine components' surface. The formation of thin, adhered, continuous, and dense protective oxide prevents the diffusion of oxidizing species [4]-[6]. In order to increase the performance of protective oxide, reactive elements such as yttrium or zirconium are added to the coating powder.

The oxidation resistance is significantly affected by porosity due to the pores acting as the diffusion paths and allowing the oxidation species to penetrate and attack the coating and substrate [6]-[10]. One of the factors which influenced the porosity level is particle size. Reducing the particle size could reduce the level of porosity. Daroonparvar et al., investigated the effect of particle size on bond coat layer [11]. Particle size reduction using the mechanical milling and alloying method caused the formation of a continuous and dense alumina layer on the sample surface [12]-[14]. However, the dry milling method produced the agglomeration of powder. Thus, the particle size increased to 120 µm from 20 µm of the initial powder. Agglomeration conditions make the particles coarser and could be a barrier to the deposition process by blocking the nozzle gun and the high porosity level of coating.

DOI : 10.55981/metalurgi.2023.713

Furthermore, Biyik and Aydin et al., studied mechanical milling parameters. The study used stearic acid in a wet milling method as a process control agent (PCA) [15]. The results obtained particle sizes of less than 35 μm, and the powder shape was flaky. PCA adsorbs the powder particles' surface and avoids the agglomeration of powder particles [16]. Ethanol was used as PCA, which could reduce the intensity of cold welding of the powder and cause flake-shaped and irregular powder formation [17].

On the other hand, characteristic of a high-energy ball mill involves deformation, fragmentation, cold welding, and structural changes such as a decrease in crystallite size and an increase in lattice strain in deformed powder. The formation of linear defects leads to a reduction in crystallite size. The crystallite size is crucial in the composite powder to evaluate its properties. The crystallite size and lattice strain are frequently calculated using integral breadth methods for line profile analysis of XRD (x-ray diffraction) peaks [18]-[19].

The simplest method used to calculate the crystallite size is Scherer's formula. However, it is applicable only when there is no strain on the materials. Other analytical methods, such as WH (Williamson hall) analysis, are generally used to determine the strain and the crystallite size of materials. It uses any peaks at lower diffraction angles to get the same information. In addition, the WH analysis is easy and suitable for strain and crystallite size calculation of cubic crystals [19]-[21].

Therefore, in this study, a combination of dry and wet milling methods was carried out to minimize the agglomeration of the powder and obtain finer particle and crystallite size. By doing these two methods, the time to reduce the size of the crystals in the powder is also shorter. The structural changes, such as crystallite size and lattice strain, were also evaluated to understand the effect of dry and wet milling combinations and the addition of the reactive element effect.

2. MATERIALS AND METHODS

2.1 Synthesis of Coating Powder

The NiCrAlY and NiCrAlZr coating powders used in the present investigation were used commercially available pure Ni, Cr, Al, Y, and Zr powder with chemical composition given in Table 1.

The mechanical milling processes were conducted in two steps: dry milling for 36 hours and wet milling for 1 hour. The wet milling was performed under ethanol to avoid the agglomeration effect. The experiment was conducted at room temperature. A planetary ball miller (SFM-1 Desk-Top) was used to synthesize fine powders with a weight ratio of ball-to-powder of 10:1 and ball diameters of 10 mm. The revolution speeds of dry and wet milling were 1500 rpm and 1200 rpm, respectively. Some abbreviations were used in this study, such as XM, DM, and WM, which were unmilled, dry milled, and wet milled powder, respectively.

Table 1. Chemical composition of NiCrAlX powders

Coating powder	Composition (wt.%)				
	Ni	Cr	Al	Y	Zr
NiCrAlY	Bal	24	7	0.4	-
NiCrAlZr	Bal	24	7	-	0.4

2.2 Characterization

A PSA (particle size analyzer) Cilas 1190 was used to characterize the powder particle size. XRD Rigaku SmartLab (x-ray diffraction) using Cu-Kα radiation that was operated at 40 kV and 30 mA for 2θ range of 10° to 90° was used to evaluate the phase analysis of unmilled and milled powders. The FE-SEM (field emission-scanning electron microscope) JEOL JEM 2010F equipped with EDS (energy dispersive spectroscopy) Oxford X-Max 50 mm^2 was used to characterize the microstructure and composition of powders.

3. RESULT AND DISCUSSION

3.1 Powders Morphology

The composites of NiCrAlY and NiCrAlZr powders have been prepared by mechanical milling. Figure 1 shows the SEM (scanning electron microscope) images associated with EDS (energy dispersive spectroscopy) results of unmilled and milled powders. The unmilled powder in Figs. 1(a), and 1(d) consisted of nickel, chromium, and aluminum particles. The nickel particle was spherical; chromium and aluminum were blocky shapes. After dry milling for 36 hours, the powder SEM images, as shown in Figs. 1(b), and 1(e) showed particle powder agglomerated with irregular morphology. The agglomeration occurred because aluminum and nickel showed high ductility and flattened, resulting in cold welding [16]. According to EDS analysis, the elemental composition of the particles was uniform. It indicates that the particles mixed, forming the composite particles. Then, the wet milling method presented in Figs. 1(c), 1(f) led to flake-shaped and irregular powders forming. The flakiness of the particles after the wet milling process for 1 hour indicates that the fracturing and fragmenting stage has occurred. In addition, the presence of ethanol as

PCA could reduce the intensity of cold welding [17]. When the fragmentation rate starts to dominate over cold welding, powder refinement occurs [20]. The grain refining was led by the severe plastic deformation of particles and accumulated internal stress [19]. Based on the EDS point analysis, a homogenized distribution of elements was observed in the milled powders. The rare earth elements, i.e., yttrium and zirconium, were not observed on the EDS analysis due to the small concentration of those elements in the composite powders. This mechanical milling process formed polycrystals on the particles.

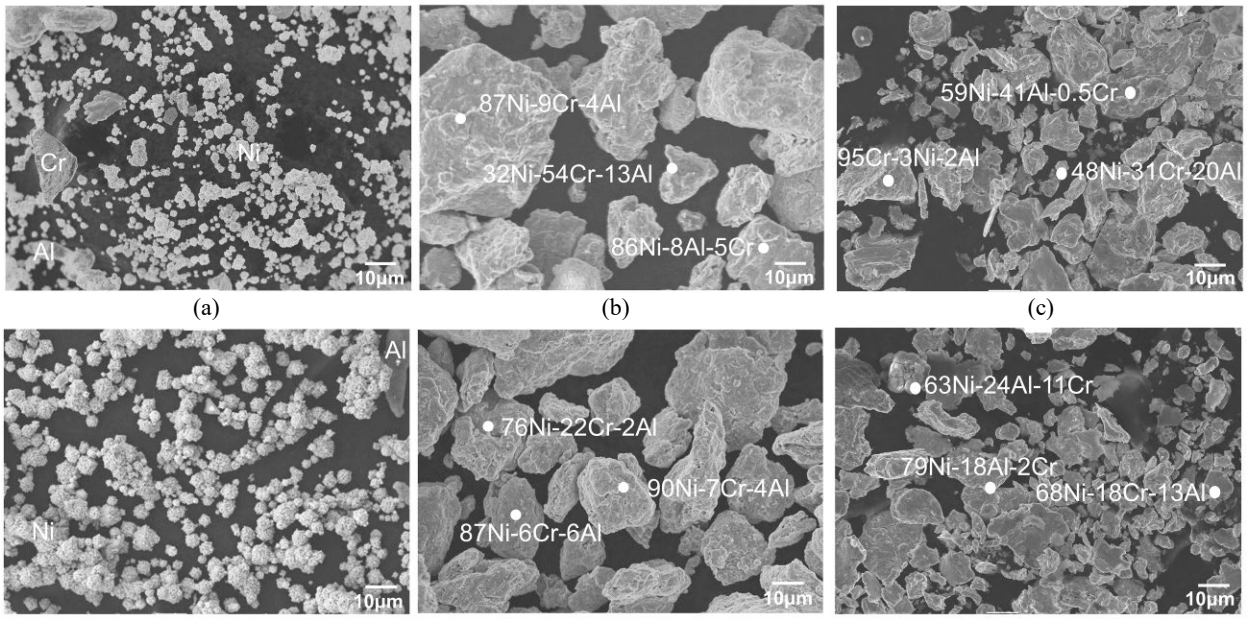

Figure 1. SEM image and EDS analysis (at%) of (a) unmilled NiCrAlY, (b) dry milled NiCrAlY, (c) dry milled followed by wet milling NiCrAlY, (d) unmilled NiCrAlZr, (e) dry milled NiCrAlZr, (f) dry milled followed by wet milling NiCrAlZr

3.2 Particle Size Distribution

Figure 2 exhibits the particle size distribution of unmilled and milled powders. The unmilled powder shows the broad particle size distribution from the small to the bigger size. The mean size of both unmilled powders was approximately 35 μm.

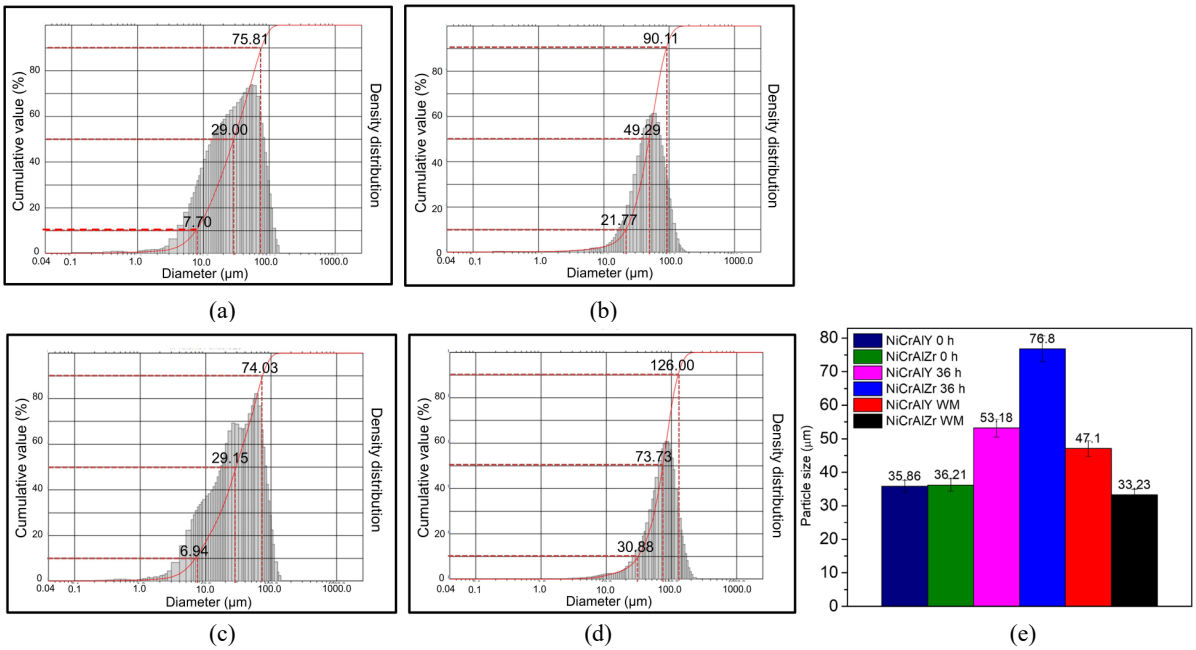

Figure 2. Particle size distribution of unmilled powder (a) NiCrAlY (c) NiCrAlZr, dry milled for 36 h of (b) NiCrAlY (d) NiCrAlZr, and average particle size of unmilled and milled powders

The dry milling process exhibited a bigger size of powders than unmilled powders. The particle distribution became narrower at the big particle size. The particle size of dry-milled powders increased up to 20-40 µm. NiCrAlZr powder showed a bigger particle size than NiCrAlY powder, approximately 53.18 µm and 76.80 µm, respectively. The fragmentation occurred after the wet milling process, resulting in a significant decrement in particle size by about 60%. It forms the flake shape particles of NiCrAlY and NiCrAlZr powders with an approximate size of 24.5 µm and 18.5 µm, respectively. SEM images presented in Fig. 1 are in correlation with the results.

3.3 Phase Identification

The XRD (x-ray diffraction) patterns of the unmilled, dry-milled, and wet-milled NiCrAlY and NiCrAlZr powders are shown in Fig. 3.

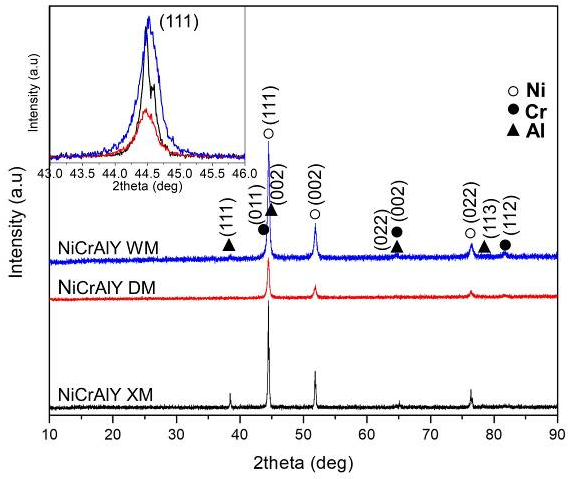

(a)

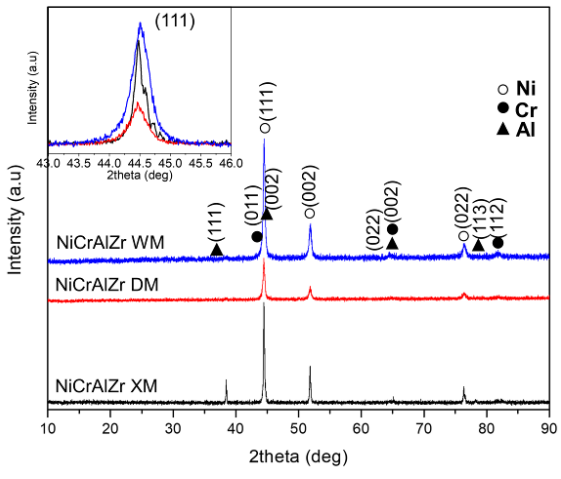

(b)

Figure 3. XRD patterns of unmilled and milled (a) NiCrAlY, (b) NiCrAlZr powders. The inset XRD pattern shows the broadening peak of the 43-46° region

The unmilled powder shows the peaks of major elements (Ni, Cr, and Al). As observed on EDS analysis, the XRD (x-ray diffraction) spectra did not detect reactive elements of yttrium and zirconium. It was due to the low composition of those reactive elements. The figure shows that the intensity of the dry-milled powder's peaks significantly decreased. Moreover, the Al peaks did not disappear on dry-milled powders. It assures that a solid solution in Ni was formed. which affects the lattice parameter of those powders [20].

In addition, the decrement in peak intensity observed on powders was due to the stress caused by mechanical milling, which generates the lattice strain. The peak intensity became high after the wet milling process, which might be due to the refinement of the crystal structure. Moreover, the diffraction line of the milled powder slightly increased the FWHM (full width at half maximum), indicating a reduction of crystallite size during mechanical milling. The inset region shows the broadening peak and the peak intensity change observed on the milled powder. The peak broadening was evaluated to calculate powders' the crystallite size and lattice strain.

3.4 X-ray Peak Broadening

To investigate the microstructural change in NiCrAlY and NiCrAlZr composite powder, the X-ray peak broadening of powders was evaluated. The broadening peaks resulting from the mechanical milling process are due to the reduction in crystallite size and the increased lattice strain caused by dislocation [22]. The diffraction peak corresponding to the instrumental corrected broadening β_{hkl} was estimated using the equation.

$$\beta_D = \{(\beta_{hkl})^2_{measured} - (\beta_{hkl})^2_{instrumental}\}^{1/2} \quad (1)$$

Scherrer's formula and Williamson-Hall's method were used to determine the crystallite size and lattice strain. These methods used the broadening of the significant element peaks, nickel peaks.

3.4.1 Williamson-Hall Analysis

The calculation of peak broadening using Scherrer's formula to measure crystallite size does not consider the strain present in the materials. However, the mechanical milling affected the XRD peak broadening due to the crystallite size and lattice strain. The crystallite size and the lattice strain contributions to peak

broadening are independent [19]. Scherrer's formula is presented in Eq. 2 [21].

$$D = \frac{k\,\lambda}{\beta_D \cos\theta_{hkl}} \quad (2)$$

where D is crystallite size, k is Scherrer constant (0.9), λ is the wavelength of CuKα radiation (1.5406 Å), β_{hkl} is the full width at half maximum (FWHM) in radians, θ_{hkl} is Bragg's angle of diffraction lines.

3.4.1.1 Uniform Deformation Model

Strain-induced broadening arising from defects like imperfections and distortions are related by Eq. (3).

$$\varepsilon \sim \frac{\beta_D}{\tan\theta_{hkl}} \quad (3)$$

The WH analysis is suitable for calculating the crystallite size and lattice strain. Since the crystallite size and lattice strain could independently affect the peak broadening, the strain-induced peak broadening β_s is given by the relation:

$$\beta_s = 4\,\varepsilon \tan\theta \quad (4)$$

$$\beta_{hkl} = \beta_D + \beta_s \quad (5)$$

$$\beta_{hkl} = \frac{k\,\lambda}{D\cos\theta_{hkl}} + 4\,\varepsilon \tan\theta \quad (6)$$

$$\beta_{hkl}\cos\theta = \frac{k\,\lambda}{D} + 4\,\varepsilon \sin\theta \quad (7)$$

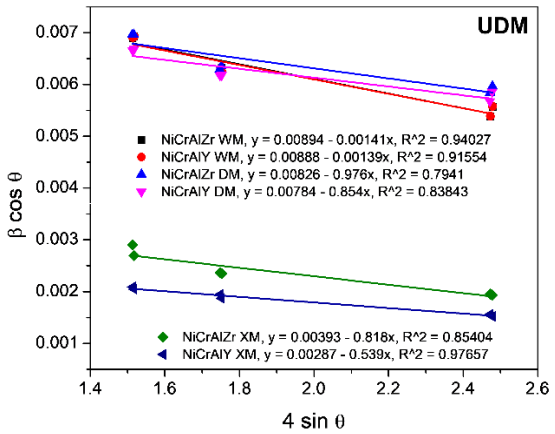

Figure 4. The Williamson-Hall analysis of unmilled and milled NiCrAlY and NiCrAlZr powder using UDM assumption

Eq. (7) represents the UDM (uniform deformation model). The plot is drawn between $\beta\cos\theta$ and $4\sin\theta$. The crystallite size and lattice strain are derived from the intercept ($c = k\lambda/t$) and the slope ($m = \varepsilon$), respectively. The UDM equation assumed that strain was uniform in all crystallographical directions. In addition, this calculation considers the isotropic nature of the crystal, which the properties of materials do not depend on the direction. The W-H analysis using the UDM assumption is presented in Fig. 4. Meanwhile, the calculation of crystallite size and lattice strain using the UDM assumption is shown in Table 2.

3.4.1.2 Uniform Stress Deformation Model

UDM considers uniform strain present in all crystallographic directions. The strain of mechanical milling powders, on the other hand, is not uniform in all directions. USDM (uniform stress deformation model) generalized Hooke's law refers to the lattice strain. The strain and stress are in linear proportionality.

$$\sigma = E_{hkl}\,\varepsilon \quad (8)$$

where σ is the stress, E_{hkl} is the modulus of elasticity, and ε is the strain.

The modulus of elasticity of the cubic FCC (faced center cubic) crystal along the direction of (h k l) is

$$\frac{1}{E_{hkl}} = S_{11} - 2(S_{11} - S_{12} - 0.5S_{44})(h^2k^2 + k^2l^2 + l^2h^2)/(h^2 + k^2 + l^2)^2 \quad (9)$$

where S_{11}, S_{12}, and S_{44} are the elastic compliances of pure Ni with values of 7.34 × 10^{-3}, 2.74 × 10^{-3}, and 8.02 × 10^{-3} GPa^{-1}, respectively. The y-intercept of $\beta_{hkl}\cos\theta_{hkl}$ versus $4\sin\theta_{hkl}/E_{hkl}$ graph, the uniform stress (σ) and the lattice strain (ε), which are derived from the slope of the mentioned graph, can be used to determine the crystallite size (D). The USDM model for unmilled and milled powder calculation is exhibited in Fig. 5. The value of crystallite size, stress, and the lattice strain estimated by USDM is presented in Table 2. A minor strain can be validly estimated using this equation.

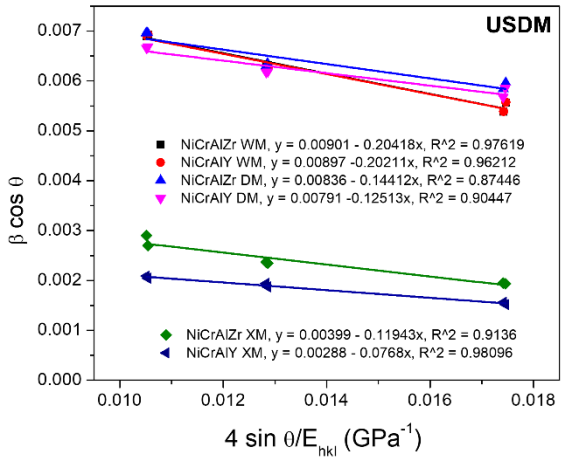

Figure 5. The Williamson-Hall analysis of unmilled and milled NiCrAlY and NiCrAlZr powder assuming USDM

3.4.1.3 Uniform Deformation Energy-Density Model

In USDM, it considers a linear proportionality between stress and strain. However, it no longer remains linear when the strain energy density (u) is considered. In the UDEDM (uniform deformation energy-density model), the cause of anisotropic strain is assumed to be deformation energy density (energy per unit). The energy density for an elastic system following Hooke's law can be determined from $u = (\varepsilon^2 E_{hkl})/2$. Then according to the energy and strain relation, the equation can be modified as presented in Eq. 10.

$$\beta_{hkl} \cos\theta = \left(\frac{k\lambda}{D}\right) + \left(4 \sin\theta \left(\frac{2u}{E_{hkl}}\right)^{1/2}\right) \quad (10)$$

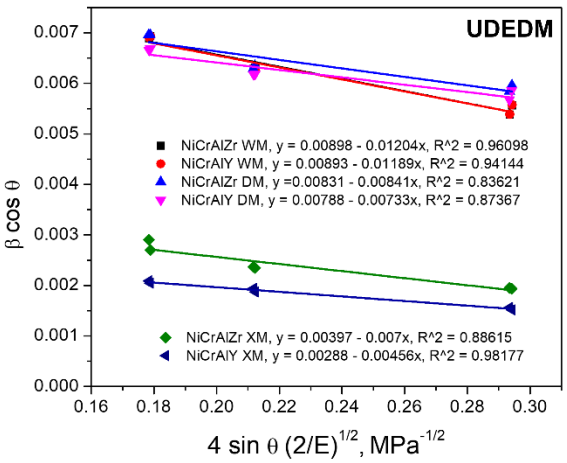

Figure 6. The Williamson-Hall analysis of unmilled and milled NiCrAlY and NiCrAlZr powder assuming UDEDM

The UDEDM graph was constructed of $\beta_{hkl} \cos\theta$ versus $4 \sin\theta \left(\frac{2u}{E_{hkl}}\right)^{1/2}$. The intercept used to determine the crystallite size (D) was calculated from the intercept, the slope of the line used to determine the anisotropic energy density and the lattice strain. The crystallite size and energy density are exhibited in Table 2.

According to the previous studies, in which crystallite size was determined using the Williamson-Hall method and then compared with the TEM (transmission electron microscope) image, the UDEDM anisotropy model could be a suggested realistic model, especially for milled powders.

Williamson-Hall's model of unmilled and milled NiCrAlY and NiCrAlZr showed a negative slope, indicating a negative strain, which might be due to the lattice shrinkage [23]. The crystallite size of milled powders calculated using UDM, USDM, and UDEDM shows the decrement. The crystallite size decrement of dry milled powder is up to 64%, from approximately 50 nm to 18 nm. Meanwhile, the difference in crystallite size of dry-milled and wet-milled powder was about 1 nm, and wet milled powder showed a smaller crystallite size. The formation of linear defects induces the reduction of crystallite size [19].

In contrast, increasing the milling time causes an increase in lattice strain. The crystal imperfection, such as point defect and dislocation, affects the lattice strain. It was due to the high-energy collision between the ball mill and vial in the mechanical milling process [24]. The stress and deformation energy also increases with the increase of milling time.

Table 2. Crystallite size and lattice strain of NiCrAlY and NiCrAlZr powders

Sample condition	Williamson-Hall method							
	UDM		USDM			UDEDM		
	D, nm	ε (×10-3)	D, nm	σ (10^{-1} GPa)	ε (x10^{-3})	D, nm	u, kJ/m^3	ε (×10^{-3})
NiCrAlY XM	50.46±0.99	0.54±0.04	50.28±2.18	0.768±0.048	0.53±0.03	50.28±2.24	0.021±0.007	0.54±0.01
NiCrAlZr XM	36.85±0.50	0.82±0.15	37.13±8.64	1.190±0.163	0.83±0.11	36.48±0.56	0.049±0.001	0.83±0.13
NiCrAlY DM	18.47±0.45	0.87±0.16	18.31±0.58	1.251±0.180	0.87±0.13	18.57±0.51	0.049±0.002	0.83±0.15
NiCrAlZr DM	17.53±0.34	0.97±0.17	17.32±0.43	1.441±0.241	1.00±0.07	17.48±0.38	0.071±0.003	0.99±0.19
NiCrAlY WM	16.31±0.39	1.39±0.19	16.14±0.58	2.021±0.179	1.40±0.12	17.88±0.47	0.141±0.002	1.40±0.16
NiCrAlZr WM	16.20±0.47	1.41±0.16	16.07±0.73	2.042±0.142	1.42±0.10	16.13±0.57	0.145±0.001	1.41±0.03

4. CONCLUSION

NiCrAlY and NiCrAlZr powders have been synthesized using a mechanical milling process resulting in a homogenous powder and were characterized by XRD (x-ry diffraction), PSA (particle size analysis), and SEM (scanning electron microscope). The mechanical milling process was divided into two stages: dry and wet. The dry milling process produced the agglomerated NiCrAlX powders. The particle size value of the is approximately 70 μm due to the high ductility of the element. The wet milling process using ethanol as a process control agent could reduce the particle size significantly up to ±30 μm.

After dry milling for 36 hours, followed by wet milling for 1 hour, the phase change of the powder did not occur. However, the disappearance of the Al peak was observed in dry-milled powder, assuming due to the solid solution formation. The dominant element of Ni shows the FCC (face centered cubic) structure. The evaluation of the dominant element broadening peak was done by W-H analysis. XRD patterns of milled powder exhibited the line broadening due to the reduction in crystallite size and increased lattice strain. The values of crystallite size and lattice strain of milled NiCrAlY and NiCrAlZr were approximately 16 nm and 1.4×10-3, respectively. The influence of reactive element addition on the powder's crystallite size and lattice strain is not observed. In conclusion, the mechanical milling process produces good powder coating characteristics, leading to good coating performance.

ACKNOWLEDGMENT

The authors would like to thank the research project from the National Research and Innovation Agency (BRIN) with contract No. 3/III.10/HK/2023 for supporting the present research work.

REFERENCES

[1] F. Ghadami, A. S. R. Aghdam, and S. Ghadami, "Microstructural characteristics and oxidation behavior of the modified MCrAlX coatings: A critical review," *Vacuum*, vol. 185, 2021. Doi: 10.1016/j.vacuum.2020.109980.

[2] Y. Huang, Y. He, B. Yang, A. Khan, X. Zhao, and P. Song, "Effect of YSZ/TaSi2-MCrAlY thermal barrier coatings on oxidation resistance in air and water vapor," *Ceram. Int.*, vol. 49, pp. 14551-14562, 2023. Doi: 10.1016/j.ceramint.2023.01.045.

[3] J. G. Thakare, C. Pandey, M. M. Mahapatra, and R. S. Mulik, "Thermal barrier coatings-A state of the art review," *Met. Mater. Int.*, vol. 27, no. 7, pp. 1947-1968, 2021. Doi: 10.1007/s12540-020-00705-w.

[4] K. M. Doleker, Y. Ozgurluk, and A. C. Karaoglanli, "TGO growth and kinetic study of single and double layered TBC systems," *Surf. Coatings Technol.*, vol. 415, 2021. Doi: 10.1016/j.surfcoat.2021.127135.

[5] A. Sezavar, S. A. Sajjadi, A. Babakhani, R. L. Peng, and K. Yuan, "Oxidation behavior of a nanostructured compositionally graded layer (CGL) thermal barrier coating (TBC) deposited on IN-738LC," *Surf. Coatings Technol.*, vol. 374, no. March, pp. 374-382, 2019. Doi: 10.1016/j.surfcoat.2019.06.024.

[6] B. J. Harder, "Oxidation performance of Si-HFO_2 environmental barrier coating bond coats deposited via plasma spray-physical vapor deposition," *Surf. Coatings Technol.*, vol. 384, pp. 2-9, 2020. Doi: 10.1016/j.surfcoat.2019.125311.

[7] S. K. Essa, K. Chen, R. Liu, X. Wu, and M. X. Yao, "Failure mechanisms of APS-YSZ-CoNiCrAlY thermal barrier coating under isothermal oxidation and solid particle erosion," *J. Therm. Spray Technol.*, vol. 30, no. 1-2, pp. 424-441, 2021. Doi: 10.1007/s11666-020-01124-4.

[8] J. Shi, T. Zhang, B. Sun, B. Wang, X. Zhang, and L. Song, "Isothermal oxidation and TGO growth behavior of NiCoCrAlY-YSZ thermal barrier coatings on a Ni-based superalloy," *J. Alloys Compd.*, vol. 844, p. 156093, 2020. Doi: 10.1016/j.jallcom.2020.156093.

[9] D. H. Kim, K. K. Kim, B. W. Moon, K. B. Park, S. Park, and C. S. Seok, "Prediction of growth behavior of thermally grown oxide considering the microstructure characteristics of the top coating," *Ceram. Int.*, vol. 47, no. 10, pp. 14160-14167, 2021. Doi: 10.1016/j.ceramint.2021.02.003.

[10] G. An, W. Li, L. Feng, B. Cheng, Z. Wang, Z. Li, and Y. Zhang, "Isothermal oxidation and TGO growth behaviors of YAG/YSZ double-ceramic-layer thermal barrier coatings," *Ceram. Int.*, vol. 47, no. 17, pp. 24320-24330, 2021. Doi: 10.1016/j.ceramint.2021.05.144.

[11] M. S. Hussain and M. Daroonparvar, "The

synthesis of nanostructured NiCrAlY powders for plasma sprayed thermal barrier coatings," *Adv. Phys. Theor. dan Appl.*, vol. 13, pp. 1-9, 2013.

[12] J. Lu, Y. Chen, H. Zhang, C. Zhao, X. Zho, F. Guo, and P. Xiao, "Superior oxidation and spallation resistant NiCoCrAlY bond coat via homogenizing the yttrium distribution," *Corros. Sci.*, vol. 159, 2019. Doi: 10.1016/j.corsci.2019.108145.

[13] H. Vasudev, L. Thakur, A. Bansal, H. Singh, and S. Zafar, "High temperature oxidation and erosion behaviour of HVOF sprayed bi-layer Alloy-718/NiCrAlY coating," *Surf. Coatings Technol.*, vol. 362, pp. 366-380, 2019. Doi: 10.1016/j.surfcoat.2019.02.012.

[14] A. Zakeri, E. Bahmani, A. S. R. Aghdam, B. Saeedi, and M. Bai, "A study on the effect of nano-CeO2 dispersion on the characteristics of thermally-grown oxide (TGO) formed on NiCoCrAlY powders and coatings during isothermal oxidation," *J. Alloys Compd.*, vol. 835, p. 155319, 2020. Doi: 10.1016/j.jallcom.2020.155319.

[15] S. Biyik and M. Aydin, "Characterization of nanocrystalline Cu25Mo electrical contact material synthesized via ball milling," *Acta Phys. Pol. A*, vol. 132, no. 3, pp. 886-888, 2017. Doi: 10.12693/APhysPolA.132.886.

[16] C. Suryanarayana, "Mechanical alloying: a novel technique to synthesize advanced materials," *Research*, vol. 2019, p. 4219812, 2019. Doi: 10.34133/2019/4219812.

[17] A. Zakeri, F. Ghadami, A. S. Rouhaghdam, and B. Saeedi, "Study on production of modified MCrAlY powder with nano oxide dispersoids as HVOF thermal spray feedstock using mechanical milling," *Mater. Res. Express*, vol. 7, no. 1, p. 015030, 2019. Doi: 10.1088/2053-1591/ab6121.

[18] A. A. Eze, E. R. Sadiku, W. K. Kupolati, J. Syman, J. M. Ndambuki, T. Jamiru, M. O. Durowoju, I. D. Ibrahim, M. B. Shongwe, and D. A. Desai., "Wet ball milling of niobium by using ethanol, determination of the crystallite size and microstructures," *Sci. Rep.*, vol. 11, no. 1, pp. 1-8, 2021. Doi: 10.1038/s41598-021-01916-w.

[19] S. Sivasankaran, K. Sivaprasad, R. Narayanasamy, and P. V. Satyanarayana, "X-ray peak broadening analysis of AA 6061100-x-x wt.% Al_2O_3 nanocomposite prepared by mechanical alloying," *Mater. Charact.*, vol. 62, no. 7, pp. 661-672, 2011. Doi: 10.1016/j.matchar.2011.04.017.

[20] D. Singh and R. Kumar, "Synthesis and characterization of nanocrystalline Ni-Cr-Al alloy powder," *Mater. Today Proc.*, vol. 41, pp. 821-824, 2020. Doi: 10.1016/j.matpr.2020.09.155.

[21] P. S. Sundaram, T. Sangeetha, S. Rajakarthihan, R. Vijayalaksmi, and A. Elangovan, "XRD structural studies on cobalt doped zinc oxide nanoparticles synthesized by coprecipitation method : Williamson-Hall and size-strain plot approaches," *Phys. B Phys. Condens. Matter*, vol. 595, p. 412342, 2020. Doi: 10.1016/j.physb.2020.412342.

[22] R. Kumar, S. R. Bakshi, J. Joardar, S. Parida, V. S. Raja, and R. K. Singh Raman, "Structural evolution during milling, annealing, and rapid consolidation of nanocrystalline Fe-10Cr-3Al powder," *Materials (Basel).*, vol. 10, no. 3, pp. 25-27, 2017. Doi: 10.3390/ma10030272.

[23] A. K. Zak, W. H. Abd. Majid, M. E. Abrishami, and R. Yousefi, "X-ray analysis of ZnO nanoparticles by Williamson-Hall and size-strain plot methods," *Solid State Sci.*, vol. 13, no. 1, pp. 251-256, 2011. Doi: 10.1016/j.solidstatesciences.2010.11.024.

[24] H. Irfan, K. M. Racik, and S. Anand, "Microstructural evaluation of CoAl2O4 nanoparticles by Williamson–Hall and size–strain plot methods," *J. Asian Ceram. Soc.*, vol. 6, no. 1, pp. 54-62, 2018. Doi: 10.1080/21870764.2018.1439606.

Metalurgi (2023) 2: 49 - 56

METALURGI
Majalah Ilmu dan Teknologi
p-ISSN 0126-3188 | e-ISSN 2443-3926
ejurnalmaterialmetalurgi.lipi.go.id

THE EFFECT OF BAKELITE BINDERS ON MAGNETIC PROPERTIES AND HARDNESS VALUES OF MQP-TYPE BONDED NdFeB MAGNETS

Lia Aryani[a], Bintang Surya Bhakti[a], Ahmad Riziq Mubarok[a], Ardita Septiyani[b], Henny Mulyani[a], Nanang Sudrajat[b], Dedi[a,b,*]

[a]Metallurgical Engineering, Jenderal Achmad Yani University
Jl. Terusan Gatot Subroto, Bandung, Indonesia 40285
[b]Research Center for Advanced Materials, National Research and Innovation Agency
KST Samaun Samadikun, Jl. Sangkuriang-Cisitu, Bandung, Indonesia 40135
*E-mail: dedi011@brin.go.id

Received: 25-05-2023, Revised: 27-09-2023, Accepted: 30-09-2023

Abstract

Permanent magnets are important in modern society as components in various devices used by many industries and consumers, especially in generators and electric motors. Bonded magnet technology allows combining powdered magnetic materials with polymers as a binder to produce magnetic components that can be applied to certain applications, such as SynRM (synchronous reluctance) motors. Bonded magnets are easy to form without sacrificing their magnetic properties, which are too large, and also reduce costs, making them more effective and efficient. This paper reports the results of a study on the manufacture of bonded magnets NdFeB using bakelite binder on MQP-type NdFeB magnets with a bakelite variation of 0.5 - 2 wt.%. The characterization included testing magnetic properties with Permagraph, morphology with SEM (scanning electron microscope), and hardness values with micro Vickers hardness tester. The results of this study obtained remanence values in the range 5.53 - 6.44 kG and hardness values in the range 341.8 - 507.9 HV for NdFeB bonded magnets. According to SEM observations, the bakelite polymer matrix has successfully bound NdFeB grains, and no porosity is visible.

Keywords: *Magnet, bonded, NdFeB, bakelite*

1. INTRODUCTION

The need for minerals is increasing and diversifying with the rapid development of civilization and technology. The latest trend in the development of environmentally friendly energy and industry is using minerals as a raw material for energy sources (electric batteries), energy conversion (solar, cell, wind turbines, etc.), the defense industry, electric vehicles, other electronics industries (industry 4.0) which require several types of minerals such as rare earth metals, lithium, cobalt, nickel, manganese, tin, graphite, quartzite, and others [1].

Rare earth metals are one of the strategic minerals. They are included in the critical minerals which consist of a collection of elements such as scandium (Sc), lanthanum (La), cerium (Ce), praseodymium (Pr), neodymium (Nd), promethium (Pm), samarium (Sm), europium (Eu), gadolinium (Gd), terbium (Tb), dysprosium (Dy), holmium (Ho), erbium (Er), thulium (Tm), ytterbium (Yb), lutetium (Lu) and yttrium (Y). These elements play a vital role in developing of technology-based advanced industries [1].

The use of these rare earth metals triggers the development of new materials. New materials using REEs provide significant technological developments in materials science. The result of this material is widely used in industry to improve the quality of products, such as magnets[1].

Rare earth metal permanent magnets have much higher magnetic properties than the previous types of permanent magnets, where the (BH)max of this type of magnet reaches 30-35 MGOe or 240 – 280 kJ.m-3. As a permanent magnet with a high energy density as indicated by the (BH)max value, this type of permanent magnet becomes a permanent magnet capable of

DOI : 10.55981/metalurgi.2023.718

Metalurgi is Sinta 2 Journal (https://sinta.ristekbrin.go.id/journals/detail?id=3708) accredited by Ministry of Research & Technology, Republic Indonesia

meeting the demands of today's technological products. These namely products prioritize space miniaturization [2].

Magnets have become an essential part of everyday life, and many applications can be applied to devices such as electric motors, loudspeakers, microwaves, telecommunications, and others [3]. Many other magnet applications are found in a miniature component in a mobile phone that relies on tiny NdFeB magnets for vibrational operation. These magnets are also often used in computer hard disk drives, where they contribute to the device by ensuring read/write positions [4]. From Figure 1, it can be seen that NdFeB magnets are widely applied to motors and generators with a percentage of 34% [5].

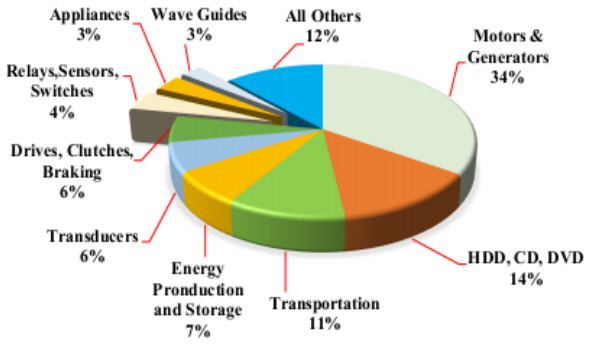

Figure 1. Proportion of Application of NdFeB Magnets [5]

The SynRM motor, or the Synchronous reluctance motor, is a 3-phase electric motor without permanent magnets and with a magnetically anisotropic rotor structure [6]. This type of motor is very popular as an electric or hybrid vehicle because of its easy and strong construction [7]. In the process, NdFeB magnets can be manufactured through powder metallurgy techniques known as bonded magnets [8]. The bonded magnet method mixes magnetic powder with polymer as a binder to produce a magnetic component [9]. The advantage of this bonded magnet is that it is easy to form without sacrificing its magnetic properties, which are too large, and reduces costs, making it more effective and efficient [10]-[11].

This study aims to improve the magnetic properties and hardness values of bonded NdFeB magnets using a bakelite binder. Through this research, it was possible to determine the effect of the bakelite binder on the magnetic properties and hardness values of the MQP-type bonded NdFeB magnets.

2. Materials And Methods

This research begins with preparing the tools and materials needed in the research process. The materials used are MQP-type NdFeB magnetic powder and bakelite polymer. In the early stages, the mass percentage estimates of the bakelite polymer to manufacture bonded NdFeB magnets was carried out. The bakelite and NdFeB powders were weighed according to previous calculations, with a total mass of 3 g per sample on the weighing paper using a spatula. After weighing, the sample is put into a plastic clip and then labeled so that the sample is not mixed up. In addition, mixing is carried out through a manual grinding process so that samples with coarse (large) grain sizes become finer (small). The weighed bakelite and NdFeB powder were mixed until homogeneous for 30 minutes using a mortar and pestle. Homogeneous samples were put into a die with a size of 12 mm and compacted using a hydraulic press. The sample was pressed with a compressive force of 10 MPa for 1 minute. The sample that comes out will be in the form of a pellet. The heating process (baking) was continued in the oven at a temperature of 250 °C for 30 minutes so that a bonded NdFeB magnet was formed.

Its physical properties (density), magnetic properties, microstructure (scanning electron microscope (SEM) - energy dispersive spectroscopy (EDS)), and hardness (micro Vickers) were then characterized. Density testing was carried out by weighing NdFeB magnets using digital scales and then measuring their dimensions using a caliper gauge so that the data obtained could be calculated using the density formula in Eq. (1).

$$\rho = \frac{m}{\pi d t^2} \qquad (1)$$

In this study, Magnet-physics Dr. Steingroever GMBH Permagraf C is a tool used to determine the magnetic properties of bonded NdFeB magnets. A sample of known density is placed in the coil so that the magnet can be read by a computer. An SEM-EDS examination was conducted to determine the NdFeB composite magnet's morphology and elemental composition. In this test, the sample was irradiated with an electron beam at a voltage of 3 kV with image magnification of 500x and 2000x. This micro Vickers test was conducted to determine the hardness of the NdFeB composite magnet. Vicker hardness tester is a tool used to measure hardness values. The load given in this study was 25 gf with a dwell time of 10 seconds.

3. RESULT AND DISCUSSION

This measurement data for bonded NdFeB magnets can be seen in Table 1.

Table 1. Dimension measurement result data

Sample (%Bakelite)	Weight (g)	d(mm)	t(mm)
0.5	2.862	12	5.18
1	2.968	12	5.44
1.5	3.042	12	5.59
2	2.968	12	5.50

In this study, bonded NdFeB magnets were in the form of pellets. Figure 2 shows that the density value per sample decreased from 4.89-4.77 g/cm^3 with increasing bakelite content.

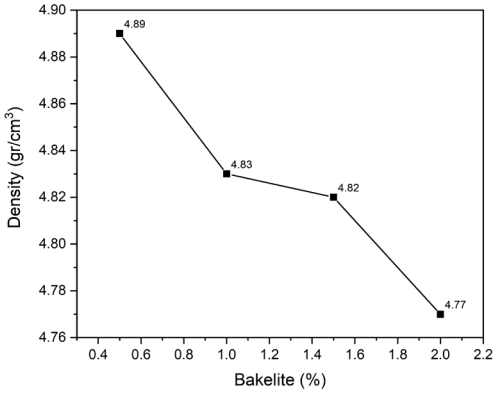

Figure 2. Graph of the relation between density and bakelite

The decrease in density indicates a reduction in sample density due to the influence of the bakelite polymer mixture on the bonded NdFeB magnet. The density of bakelite, which is 1.3 g/cm^3, is less than the density of the NdFeB magnet, which is 7.61% [12]. The highest density value is owned by a sample with 0.5% bakelite, and the smallest density value is owned by a sample with 2% bakelite. The difference between the density values obtained by the research and the theory is quite large, which can affect the magnetic properties of the bonded NdFeB magnets.

After calculating the density, permagraph testing was carried out to determine the magnetic properties of the bonded NdFeB magnets. The results obtained from this permagraph are in the form of a hysteresis curve in Fig. 3, which can provide information on the value of remanence (Br), coercivity (Hc), and maximum product energy $(BH)_{max}$. Magnetic properties data can be seen in Table 2. From Figure 3, the hysteresis curve of the bonded NdFeB magnets, it can be seen that the material is a hard magnet; this is indicated by the loop shape of the hysteresis curve, which widens considerably. The hysteresis curve shows that the wider the hysteresis curve, the higher the Coercivity is the strength of the magnetic field required to reduce the magnetization or magnetic induction to 0 from the saturation magnetization state [13]. From Figure 5, the coercivity value tends to increase with increasing bakelite. From the results of this study for a bakelite content of 1.5-2%, the coercivity value is not much different from the reference magnet of 6.032-6.06 Oe. The specification for MQP type NdFeB magnetic powder has a coercivity value of 6.5-7.5 kOe [14]. bakelite composition. The most expansive curve is found in samples with 2% bakelite. Samples with 0.5% bakelite have a smaller curve shape than other bakelite variations.

Table 2. Magnetic properties data

Sample (%Bakelite)	Br(kG)	Hc(kOe)	$(BH)_{max}$ (MGoe)
0.5	6.44	4.983	3.84
1	6.20	5.976	6.54
1.5	5.57	6.050	5.57
2	5.53	6.032	5.84

Based on the curve results, magnetic properties such as remanence Br, coercivity Hic, and energy product $(BH)_{max}$ for each sample are presented in Table 2.

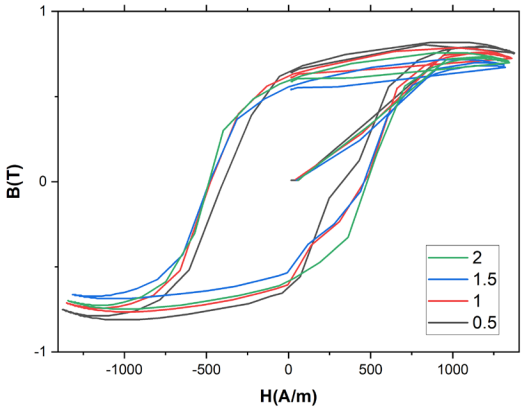

Figure 3. Hysteresis curve of the bonded NdFeB magnets with a bakelite variation of 0.5, 1, 1.5 and 2

The results show that the remanence value decreases, and the coercivity and BH_{max} values increase with each addition of bakelite composition. The bakelite composition significantly affects the Br, Hc, and $(BH)_{max}$ values.

Remanence is the residual magnetic field (B) during magnetization when the H magnetic field is removed [13]. The remanence value decreases as more bakelite is added. This is because bakelite is a non-magnetic material, so the remanence decreases as the amount of bakelite increase. From Figure 4, samples with 0.5% bakelite have the highest remanence, and samples with 2% bakelite have the lowest remanence.
Samples with 0.5% bakelite have stronger magnetic properties than samples with greater bakelite variation. The decrease in magnetic properties is due to the increase in bakelite, a polymer.

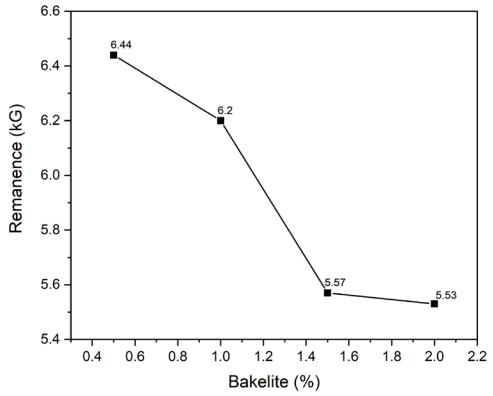

Figure 4. Graph of the remanence relation with bakelite

The greater the coercivity value of a magnet, the stronger the magnetic properties.

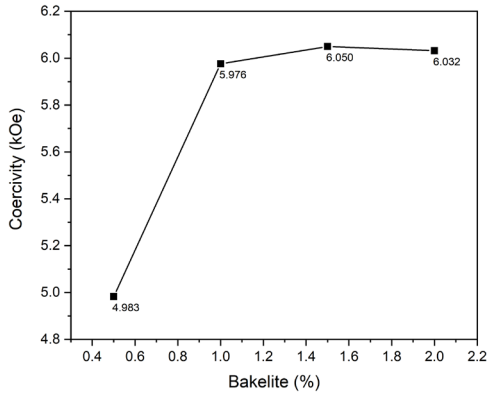

Figure 5. Graph of the coercivity of bakelite

Figure 6 shows that the $(BH)_{max}$ values increase with increasing bakelite content. It's simply that from 0.5% to 1% bakelite samples, there was a significant increase with a difference in value of 2.7 MGOe.

Several factors that can affect the magnetic properties of bonded magnets are grain size, compaction pressure, and temperature [15]. According to research by A. Ritawanti et al., the larger the grain size, the stronger the magnetic properties.

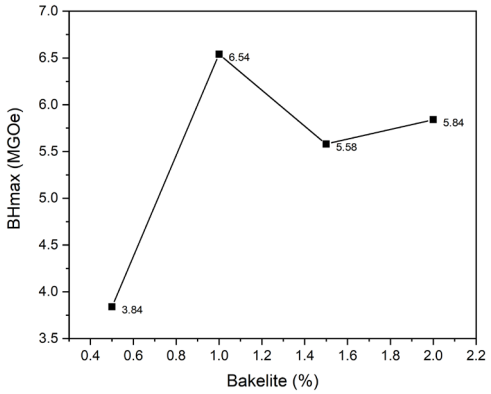

Figure 6. Graph of the relation between BH $_{max}$ and bakelite

The formation of porosity due to grain size can affect the density value; if it does not approach the theoretical density value, then the magnetic properties will not be appropriate [16]. If the temperature applied exceeds the curie temperature, the magnetic properties will be weakened [17]. In physics and materials science, the Curie temperature is the temperature at which a particular material loses its permanent magnetic properties [21]. In this study, the NdFeB bonded magnet is a ferromagnetic material that will lose its magnetic properties when it is above the curie temperature, and NdFeB bonded magnets are ferromagnetic materials that feature good loop hysteresis curves because when an external magnetic area is applied to a ferromagnet, the atomic dipoles align themselves with it. Even when the field is removed, part of the alignment will be retained: the material has become magnetized [17]. SEM-EDS (scanning electron microscope-energy dispersive spectroscopy) testing was carried out to determine the surface morphology and composition of the elements in bonded NdFeB magnets. In the SEM test, magnification was carried out two times, namely 500x magnification and 2000x magnification. The NdFeB powder in the SEM results is marked in gray, while the bakelite is marked in white.

SEM results from Fig. 7(a) 0.5% bakelite sample with 500x magnification, it can be seen in the figure that the NdFeB powder has non-uniform grain sizes; this could be due to the process of mixing the NdFeB powder and bakelite manually with a mortar and pestle where the pressure is applied at the time of grinding is different and also no sieving is done. The grain size of these samples ranged from 45-100 μm as measured directly by SEM. In the results of this image, it is clear that there are gaps between the grains; this can be caused by non-uniform grain sizes and the lack of compacting pressure used so that the sample still has a lot of porosity [18]. In addition, the increase in bakelite affects the presence of porosity [18]. Bakelite is located between the grain gaps, and the distribution of bakelite is not evenly distributed. SEM results with 2000x magnification did not show any bakelite distribution; this could be due to the small percentage of bakelite. After magnification, the presence of bakelite is not visible, as in Fig. 7(b).

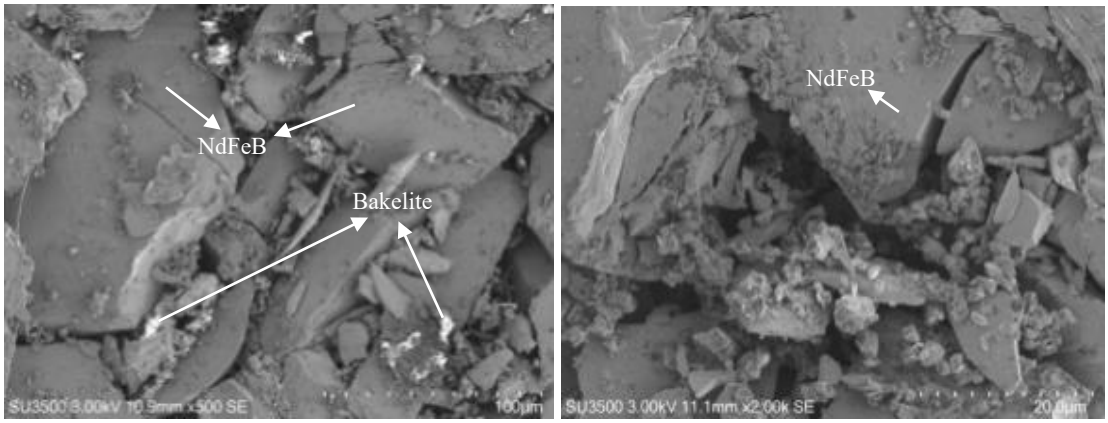

(a) (b)

Figure 7. (a) Morphology of NdFeB + bakelite 0.5%, (b) magnification area of (a)

The results of a 1% bakelite with 500x magnification demonstrate that the grain size is not homogeneous, as illustrated in Fig. 8(a). Bakelite distribution is not limited to grain gaps, and bakelite begins to appear above the surface.

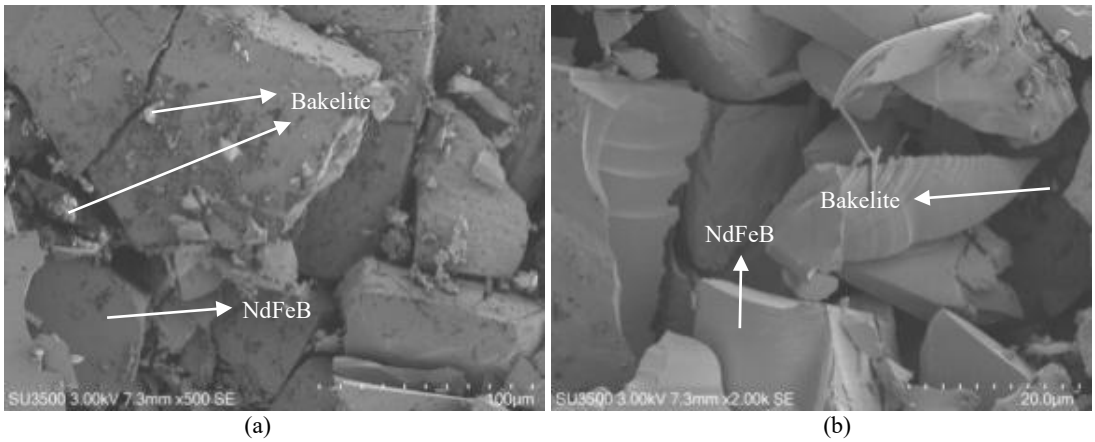

(a) (b)

Figure 8. (a) Morphology of NdFeB + 1% bakelite, (b) magnification area of (a)

In Figure 9, the presence of bakelite is not visible; a lens magnification is needed to confirm the presence of bakelite. The presence of bakelite had bonded some of the grains together, and there was a difference in grain size after magnification.

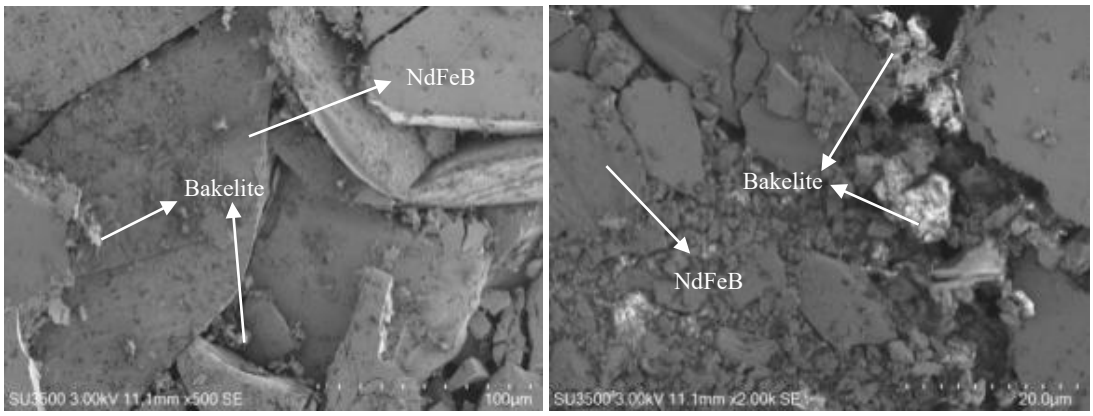

(a) (b)

Figure 9. (a) Morphology of NdFeB + bakelite 1.5%, (b) magnification area of (a)

Figure 10 shows the SEM results for the 2% bakelite sample. The image clearly shows the presence of bakelite compared to the other sample results. In Figure 10, it is very clear that evenly distributed bakelite can provide very good bonding properties [19].

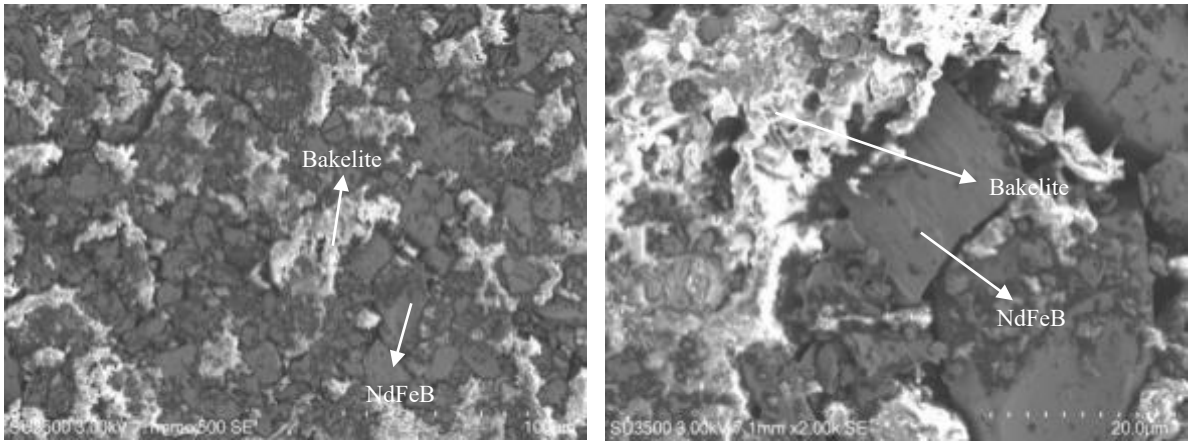

(a) (b)

Figure 10. (a) Morphology of NdFeB + bakelite 2%, (b) magnification area of (a)

During the heating process, the bakelite melts. This melted bakelite coats the surface and adhered one grain to another. The presence of bakelite is not only between grains but above the grain surface. This can happen because there is an indication that the bakelite is burning. So it can be concluded that the more bakelite, the smaller the porosity is formed because the bakelite fills the gaps between the grains, which then envelops the surface of the bonded NdFeB magnets.

Table 3 shows the result of EDS testing of 4 samples. EDS detected 9 elements. The atomic percentages of the elements Nd, Pr, and Fe tend to decrease with increasing bakelite. The EDS results showed the presence of oxygen (O) in the sample, indicating that the bonded NdFeB magnets were well oxidized [20]. From the above data, as bakelite increases, the number of carbon elements from the four samples increases from 5.53%, 7.31%, 17.22% to 44.86%. This is because bakelite is a polymer, which a cross-linked carbon chain pattern, so there is a contribution that can alter these magnetic metals.

Table 3. Elemental composition of EDS results

Element	Composition (wt.%)/% Bakelite			
	0.5	1	1.5	2
Nd	0.33	0.72	0.01	2.05
Pr	16.50	15.47	9.43	-
Fe	61.12	61.09	55.31	22.68
B	5.09	4.60	7.20	5.96
C	5.53	7.31	17.22	44.86
Co	5.96	5.16	-	-
O	3.92	4	10.84	20.21
F	5.53	1.66	-	-
Ca	-	-	-	4.14

The micro Vickers results can be seen in Table 4. From Table 4, each sample was tested at three points. So that the hardness value obtained is the result of the average, the hardness value of the bonded NdFeB magnets can be seen in Table 4.

Table 4. Micro Vickers test result

Sample (% Bakelite)	Hardness Value (HV)			
	I	II	III	Average
0.5	329.1	368.6	327.7	341.8
1	473.1	456.8	443.9	457.93
1.5	512.1	514.8	487.7	504.86
2	477.4	515.4	530.9	507.9

In this study, the sample with 2% bakelite had the highest hardness value. This is because bakelite, in its molecular structure, has excellent strength, so it can form cross-linked solid networks to increase strength during the heating process [19]. As evidenced by Figure 10(g), the results of SEM data on this sample show that the bakelite polymer is evenly distributed, which can provide excellent bonding and better mechanical properties to bind NdFeB magnets [19]. Therefore, the bakelite polymer provides good hardness properties to these bonded NdFeB magnets.

Figure 11 shows that with increasing bakelite, the hardness value of the bonded NdFeB magnets will be higher.

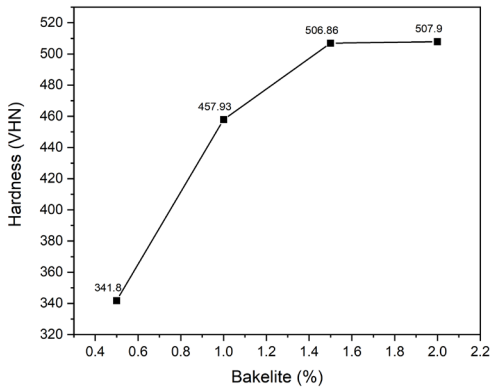

Figure 11. The effect of bakelit level on the hardness value of NdFeB

4. CONCLUSION

Conclusions from the results of the study on the effect of bakelite on the magnetic properties and hardness values of MQP-type bonded NdFeB magnets:

Bonded NdFeB magnets can be made by mixing NdFeB magnetic powder with bakelite polymer, compacting it, and then heating it. In this study, the 1% bakelite sample was optimal regarding magnetic properties, while the 2% bakelite sample was optimal regarding hardness properties. This is because the addition of bakelite is very influential. The sample with 0.5% bakelite has a high remanence value of 6.44 kG, so it can be said that this sample has a higher magnetic strength compared to the other samples. Because a significant percentage of bakelite succeeded in binding the NdFeB granules, the hardness value of 507.9 HV was higher in the NdFeB with 2% bakelite than in the others.

ACKNOWLEDGMENT

We acknowledge the Research Center for Advanced Materials, National Research and Innovation Agency (BRIN), Department of Metallurgy Engineering, Jenderal Ahmad Yani University (UNJANI), and Manufacturing Polytechnic Metal Testing Laboratory for providing several synthesis and characterization facilities.

REFERENCES

[1] E. Suwargi, B. Pardiarto, and T. Islah. "Potensi logam tanah jarang di Indonesia," *Buletin Sumber Daya Geologi*, vol. 5, no. 3, pp. 131-140, 2010. Doi: 10.47599/bsdg.v5i3.263.

[2] N. Idayanti, A. Manaf, and Dedi. "Magnet nanokomposit sebagai magnet permanen masa depan," *Metalurgi, vol.* 33, no. 1, pp. 1-18, 2018. Doi: 10.14203/metalurgi.v33i1.433.

[3] T. Kristiantoro, N. Idayanti, N. Sudrajat, A. Septiani, and Dedi,"Application of bonded NdFeB magnet for C-band circulator component," *Journal of Physics: Conference Series,* vol.776, no. 1, pp. 012030, 2016. Doi: 10.1088/1742-6596/776/1/012030.

[4] G. F. Rahman, M. A. Ikaningsih, A. Septiani, N. Sudrajat, M. A. Jabaris, "Effect of compaction pressure on microstructure and magnetic properties of $Nd_2Fe_{14}B$ alloys by powder metallurgy process," *International Conference on Radar, Antenna, Microwave, Electronics, Electronics, and Telecommunications (ICRAMET)*, pp. 99-102, 2021. Doi: 10.1109/ICRAMET53537.2021.9650488.

[5] Y. Zhang, F. Gu, Z. Su, S. Liu, C. Anderson, and T. Jiang. "Hydrometallurgical recovery of rare earth elements from NdFeB permanent magnet scrap: A review," *Metals*, vol. 10, no. 6, pp. 841, 2020. Doi: 10.3390/met10060841.

[6] P. Matyska,"Advantages of synchronous reluctance motors," *Transactions on*

Electrical Engineering, vol. 3, no. 2, pp. 44-47, 2014.

[7] "What is synchronous reluctance motor & its working",https://www.elprocus.com/synchronous-reluctance-motor-working [accessed June. 27, 2022].

[8] Y. Yang, R. Ren, Y. Wang, L. Fang, Y. Chen, Q. Gao, L. Yang, J. Liu, X. Fang, and B. Dong, "Effect of molding pressure on structure and properties of ring-shaped bonded NdFeB magnet," *IEEE Transactions on Magnetics*, vol. 56, no. 12, pp. 1-5, 2020. Doi: 10.1109/TMAG.2020.3027438.

[9] D. Permatasari, N. Rusnaeni, M. Muljadi, E. Arif, and N. M Noer. "Pengaruh variasi% wt resin epoksi pada sifat fisis, Mikrostruktur Sifat Magnet Bonded NdFeB," *Jurnal Ikatan Alumni Fisika Universitas Negeri Medan*, vol. 2, no. 1, pp. 7-9, 2016. Doi: 10.24114/jiaf.v2i1.3512.

[10] A. R. Harahap. "Pembuatan bonded magnet NdFeB menggunakan polimer bakelit dengan cara hot press dan karakterisasinya", Doctoral Dissertation, Universitas Sumatera Utara, Indonesia, pp. 2, 2015.

[11] P. Sinuhaji, Muljadi, P. Sardjono, E. Lingga, and A. F. Piliang. "The effect of composite bonded magnet NdFeB/$BaFe_{12}O_{19}$ composition with an addition of bakelite to physical and magnetic properties," *Journal of Physics: Conference Series,* vol. 1120, no. 1, pp. 012026, 2018. Doi: 10.1088/1742-6596/1120/1/012026.

[12] Ramlan, P. Sardjono, Muljadi, D. Setiabudidaya, and F. Gulo. "Analysis of the physical, mechanical, and magnetic properties of hard magnetic composite materials NdFeB made using bakelite polymers," *Journal of Magnetics*, vol. 24, no. 1, pp. 39-42, 2019. Doi: 10.4283/JMAG.2019.24.1.039.

[13] V. A. Manik. "Pembuatan dan karakterisasi bonded magnet barium hexaferrite–neodymium iron boron dengan variasi komposisi resin epoksi", Doctoral Dissertation, Universitas Sumatera Utara, Indonesia, pp. 8-9, 2019.

[14] Magnequench leading magnet innovation. "MQP-16-7-11277-070,"www.magnequench.com [accessed July. 07, 2022].

[15] Suprapedi, Muljadi, P. Sardjono, and Ramlan. "The effect of milling time on physical properties, magnetic properties and microstructure of bonded magnet $BaFe_{12}O_{19}$," *Key Engineering Materials,* vol. 855, pp. 34-39, 2020. Doi: 10.4028/www.scientific.net/KEM.855.34.

[16] A. Ritawanti, K. Sembiring, Muljadi, and E. Y. Febrianto. "Pengaruh ukuran butir (grain size) pada pembuatan bonded magnet NdFeB," *Jurnal Ikatan Alumni Fisika Universitas Negeri Medan*, vol. 2, no. 1, pp. 10-15, 2016.

[17] L. Rohman, S. Novitasari, and Supriyadi. "Temperatur curie dan medan koersivitas material Co0.8Ni0.2 dalam struktur random alloy dan double layers," *Indonesian Journal of Applied Physics*, vol. 10, no. 1, pp. 1-7, 2020. Doi:10.13057/ijap.v10i01.31346.

[18] D. Aryanto, Z. Ray, T. Sudiro, A. S. Wismogroho, and N. Sudrajat. "The effect of powder particle size on the structural and magnetic properties of bonded NdFeB magnet," *Advanced Materials Research,* vol. 1123, pp. 88-91, 2015. Doi: 10.4028/www.scientific.net/AMR.1123.88.

[19] W. Xi, W. Liu, M. Yue, D. Zhang, Q. Lu, H. Xu, H. Zhang, Q. Wu, and Y. Li. "Preparation and characterization of phenol formaldehyde bonded Nd–Fe–B magnets with high strength and heat resistance," *IEEE Transactions on Magnetics*, vol. 54, no. 11, pp. 1-4, 2018. Doi: 10.1109/TMAG.2018.2839605.

[20] N. Rusnaeni, P. Sarjono, Muljadi and N. Noer. "The epoxy resin variation effect on microstructure and physical properties to improve bonded Ndfeb flux magnetic density," *Journal of Physics: Conference Series,* vol. 776, no. 1, pp. 012025, 2016. Doi: 10.1088/1742-6596/776/1/012025.

[21] "Curie temperature", https://en.wikipedia.org/wiki/Curie_temperature [accessed September. 9, 2023].

Metalurgi (2023) 2: 57 - 64

METALURGI
Majalah Ilmu dan Teknologi
p-ISSN 0126-3188 | e-ISSN 2443-3926
ejurnalmaterialmetalurgi.lipi.go.id

EFFECT OF HOT ROLLING AND SOLUTION TREATMENT ON THE MICROSTRUCTURE AND MECHANICAL PROPERTIES OF Fe-Mn-Si-Cr-Ni SHAPE MEMORY ALLOY

Miftakhur Rohmah[a,*], Emmanoela Carissa Sendouw[b], Rifqi Aulia Tanjung[b], Dedi Pria Utama[a], Efendi Mabruri[a]

[a]Research Center for Metallurgy, National Research and Innovation Agency
B.J. Habibie Sains and Technology Area, Banten, Indonesia 15314
[b]Department of Materials and Metallurgical Engineering, Institut Teknologi Kalimantan
Soekarno Hatta KM 15, Balikpapan, Kalimantan Timur, Indonesia, 76127
*E-mail: miftakhur.rohmah@brin.go.id

Received: 14-03-2023, Revised: 29-07-2023, Accepted: 01-08-2023

Abstract

Fe-14Mn-4Si-8Ni-11Cr SMA (shape memory alloy) was designed as a smart material because of its specific properties, which can memorize the original shape, so it has the potential to dampen vibration in seismic structures. Memory effect is triggered by SIM (stress-induced martensitic) transformation from γ-austenite to ε-martensite (hexagonal close-packed / HCP) structure, and it is recovered by heating after unloading. This study investigated the effect of hot rolling and solution treatment on the microstructure and its relationship with hardness and SME (shape memory effect) properties. The as cast of Fe-14Mn-4Si-8Ni-11Cr was hot rolled (900 and 1000 °C) and solution treated (1000 and 1100 °C). After the thermomechanical process, all microstructures consist of γ-FCC (face-centered cubic), the annealing twins, and a fine band of ε-martensite. The grain size of the γ-phase is 29.43, 41.96, 42.44, and 45.57 μm for samples B, C, D, and E, respectively. The higher the temperature of hot rolling and solution treatment applied, the larger the grain size obtained, indirectly reducing the hardness to 299.93 BHN and 286.52 BHN for samples D and E. The coarsened austenite grain, a lower number of annealing twins, and the pre-existing line band of ε-martensite are favorable to obtain the enormous recovery strain, up to 8.26% for sample E.

Keywords: *Fe-Mn-Si-Ni-Cr, SMA (shape memory alloy), SME (shape memory effect), strain recovery*

1. INTRODUCTION

Shape memory alloy is an intelligent material that can revert to its original form after deformation, which became critical for biomedical, construction, automotive, and aerospace applications. In terms of earthquake resistance construction, SMA (shape memory alloy) can dampen vibrations, reduce the destruction effect, and provide a seismic response by self-centering capabilities despite extensive deformation [1]-[2]. As a result of these desirable properties, SMA might be employed to improve the existing structures, such as beam-column connections, specific braces, pre-stressing bars, dissipation dampers, and base isolation systems. In two decades, some researchers have been interested in the development of Fe-based SMAs due to their high mechanical properties (good workability and machinability), higher thermal hysteresis, lower production preparation costs, and relatively SME (shape memory effect) when compared to NiTi-based and Cu-based [1],[3]. When Fe-Mn-Si SMA alloy is heated or loaded, the heat or stress-induced martensitic transformation from γ-austenite (face-centered cubic/FCC) to ε-martensite (hexagonal close-packed/HCP) structure and its reversion during cooling or unloaded [3]. The ability to transform reverse (FCC ⇔HCP) by generating the strain-

DOI : 10.55981/metalurgi.2023.708

induced epsilon martensite (ε-SIM) is the most appropriate indicator of SME levels.

The shape memory ability depends on the morphology and orientation of the parent phase (austenite) for its transformation site [4]. Unfortunately, the SME and recovery strain effect of polycrystalline Fe-Mn-Si was lower (2-4%) than that of single crystal (~9%) due to variations of orientation in polycrystalline caused the concurrent dislocation glide during its irreversible transformation [5]. This condition of low recovery strain can not be implemented for engineering purposes. Manufacturing a single crystal structure is very difficult for massive production on the industrial scale. Several efforts were developed to improve the shape memory effect in polycrystalline of Fe-Mn-Si based, such as employing special heat treatment (thermomechanical treatment, training, and ausforming) [3], modification of chemical composition by adding the element that can form finer precipitation (Nb, C, V, etc.) [6] and stabilize the austenite phase (Mn and Ni) [7]. Fawkhry [4] concluded that the grain size of polycrystalline SMA has two conflicting effects during the phase transformation process. Small grains produced more ε-martensite nucleation sites and more twin structures, which would hinder Shockley movement and lead to the deterioration of the SME. The more significant of twins showed the poor shape memory effect because the twins directly relate to low grain boundary energies that can't be restored by heating [8]. In contrast, Choi et al., [9] reported that the increase in grain size enhanced the volume fraction of thermally induced martensite due to the improving degree of recrystallization. The relations of variables and the effect of these studies need to be further investigated to improve performance for engineering purposes. Another study reported that thermomechanical treatment at ~600℃, particularly with rolling addition before the solution treatment, reduced the accumulated dislocation, improved the shape memory properties, developed a [111] texture in the austenite phase due to the increasing austenite stability in small grain [10]. Dynamic recrystallization activated during the rolling process at 1000 ℃ followed by annealing at 700 ℃ provides a more regularly shaped grain with low stacking fault than those by warm rolling (600 ℃), further leading the improvement of SME in the Fe-17Mn-6Si-9Cr-5Ni-0.09C and Fe-22Mn-4Si-8Cr-5Ni [8].

Other than that, the high Mn levels in Fe-Mn-Si-based SMA usually range from 15 to 30%, which is a significant concern when this alloy is to be massively produced. On the contrary, the lower Mn decreases the ε-martensite stability and increases the martensite start transformation temperature. This problem was compensated for by adding the 4-5 wt.% Ni and 5-9 wt.% Cr, and large excess Si content [8]. So, applying thermomechanical treatment with appropriate chemical composition became critical in improving the shape memory effect.

In this work, the effect of pre-rolling before solution treatment with the varied temperature of each process was subjected to correlate its impact on the microstructure and mechanical properties of Fe-14Mn-4Si-8Ni-11Cr alloy.

2. MATERIALS AND METHODS

The Fe-Mn-Si-Ni-Cr alloy with the exact chemical composition, as shown in Table 1, was melted in an induction melting furnace. The $Ni_{eq.}$ and $Cr_{eq.}$ were calculated by the Hammer equation (Eq. 1-2) [11].

$$Cr_{eq} = Cr + 1.5Si + 1.37Mo + 2Nb + 3Ti \quad (1)$$
$$Ni_{eq} = Ni + 0.31Mn + 22C + 14.2N + Cu \quad (2)$$

The cast ingot was cut to 100 x 25 x 6 mm using a wire cut machine and then homogenized at 1050 ℃ for 3 hours. Two samples were rolled to around 3 mm of thickness (65% reduction) in three passes at 900 °C and two others at 1000 °C to determine the effect of hot rolling temperature.

Table 1. Chemical composition (wt.%) of Fe-Mn-Si-Cr-Ni alloy

Fe	Mn	Si	Cr	Ni	C
Balance	14.22	3.76	10.54	8.23	0.09

Then, each varied sample was performed on the solution treatment process at 1000 and 1100 ℃ for 30 minutes in an argon environment, followed by water quenching. The sample code is summarized in Table 2.

Table 2. Description of sample code

Sample Code	Description
A	As-cast
B	Hot rolling 900 ℃ and solution treatment at 1000 ℃
C	Hot rolling 900 ℃ and solution treatment at 1100 ℃
D	Hot rolling 1000 ℃ and solution treatment at 1000 ℃
E	Hot rolling 1000 ℃ and solution treatment at 1100 ℃

The shape memory behavior on the sample processed by thermomechanical was evaluated by the degree of tensile shape recovery (Eq. 3). Each

steel was prepared as a tensile sample with a gauge length of 25 mm and diameter of 6 mm, according to ASTM E8 standard. The pre-strain (10%) with 0.5 mm/min speed loaded was provided to give stress at room temperature, followed by unloading with the same speed using Tinius Olsen Hydraulic Universal Testing Machine. Finally, all specimens were heated at 600 °C for 15 minutes in Nabertherm Muffle Furnace with an argon environment to complete the reverse transformations for the recovery process. This method was introduced by Matsumura et al., [12].

$$SME = \frac{l1-l2}{l1-l0}\ x\ 100\% \quad (3)$$

The l0, l1, and l2 are the gauge lengths on the specimen before the tensile loading, after the unloading, and after the complete reverse transformation, respectively.

A metallographic test was carried out to confirm the microstructure using an optical microscope Olympus Type BX53M. Each sample was cut to 1x1 mm by a precision cutting machine, mounted in epoxy resin, mechanically ground using SiC paper (80-1200 grit), polished with alumina slurry (5 and 1 μm), and etched to Kalling etchant (made from 5 g $CuCl_2$ + 100 mL HCl + 100 ml ethanol). The Heyn Lineal Intercept procedure (ASTM E112) calculated the grain size. The microstructure was also confirmed by XRD (x-ray diffraction) Bruker with Co-Kα source (1.789 Å). Then, the Rietveld method was used to analyze its lattice parameter phase using GSAS-II. The hardness test was performed to investigate the change in hardness value using the AFRI Hardness tester machine with Brinell methods (diameter indenter of 5 mm).

3. Result and Discussion

3.1 Microstructure analysis

Microstructure morphology before pre-strain, including the grain size of austenite and the annealing twins, feature, is crucial in determining the shape memory effect. Figure 1 shows the microstructure of Fe-14Mn-4Si-8Ni-11Cr as-cast and after thermomechanical treatment. In the ordinary optical microscope, the microstructure is a typical dendritic structure of the austenite phase. For the Fe-Mn-Si-Ni-Cr steels used in this study, Creq=16.18 wt.% and Nieq=14.62 wt.%, giving the ratio of Cr equivalent and Ni equivalent equal to 1.11, indicating the equilibrium solidification of Fe-Mn-Si-Ni-Cr follows the A modes (L → L+γ → γ) due to Mn that known as an austenite former during solidification [11].

After the thermomechanical process, the dendritic structure transformed into the fully austenitic structure with thermal twin (Figure 1b-e) and the finer slip line bands in particular grains, which were assumed to identify ε-martensite after grinding. Slightly plastic deformation in compressive stress was induced by mechanical grinding or polishing with multiplicity orientation. A consequence due to low stacking faults energy of FeMnSi SMA and the external stress during grinding, the SIM (stress-induced martensite) transformation occurred, leading the γ-FCC grains to transform into ε-martensite [13]. Its microstructure agrees with the report from other Fe-Mn-Si-Cr-Ni findings [10],[14]-[15]. Additionally, Fig. 1b shows the incomplete delineation grain boundary, possibly due to the misorientation variation [8]. Sample B exhibits a smaller grain size (29.43 μm) than Sample C (41.96 μm), suggesting that the higher solution treatment temperature provides more strain energy for completed recrystallization, migration of austenite grain boundaries, and growth during solution treatment [4][14]. With the higher temperature rolling, the grain size was increased to 42.44 μm and 45.57 μm for samples D and E, respectively. These values are higher than the sample that results in hot rolling of 900 °C, indicating the higher temperature in the rolling process increased thermal energy, which encouraged the atoms to move and form a new crystal structure [14].

Furthermore, the annealing twin with mostly straight boundary lines crossing the austenite grains is visible in sample B-E due to the lower stacking fault energy of Fe-14Mn-4Si-8Ni-11Cr during recrystallization. The annealing twin structure, as planar defects resulting in the stacking fault overlapped, was probably proposed as a growth accident, grain boundary dissociation, or the stacking fault package originates near the start of the migrating recrystallization and subsequently merged [15]-[16]. The average twin length is 90.97, 128.527, 135.23, and 160.88 μm for samples B, C, D, and E, respectively. The twin spacing of the higher temperature sample (samples C and E) is larger than that of lower temperature (samples B and D). By increasing the temperature of hot rolling and solution treatment during plastic deformation, the number of twin and stacking faults reduces, representing the densities of annealing twin boundaries and grain boundaries decreases. Still, its length increases [15],[17]. The smaller grain size provides more site for the

formation of twins since it is driven by the stored energy consumption in the grain boundary [16].

The XRD also confirms these microstructures, as shown in Fig. 2. According to the Schaeffler diagram, Fe-14Mn-4Si-8Ni-11Cr only contains a full austenite phase; however, XRD results indicate the presence of dominated γ-FCC and relatively weak intensity of ε-HCP (metastable phase) as impurities peak.

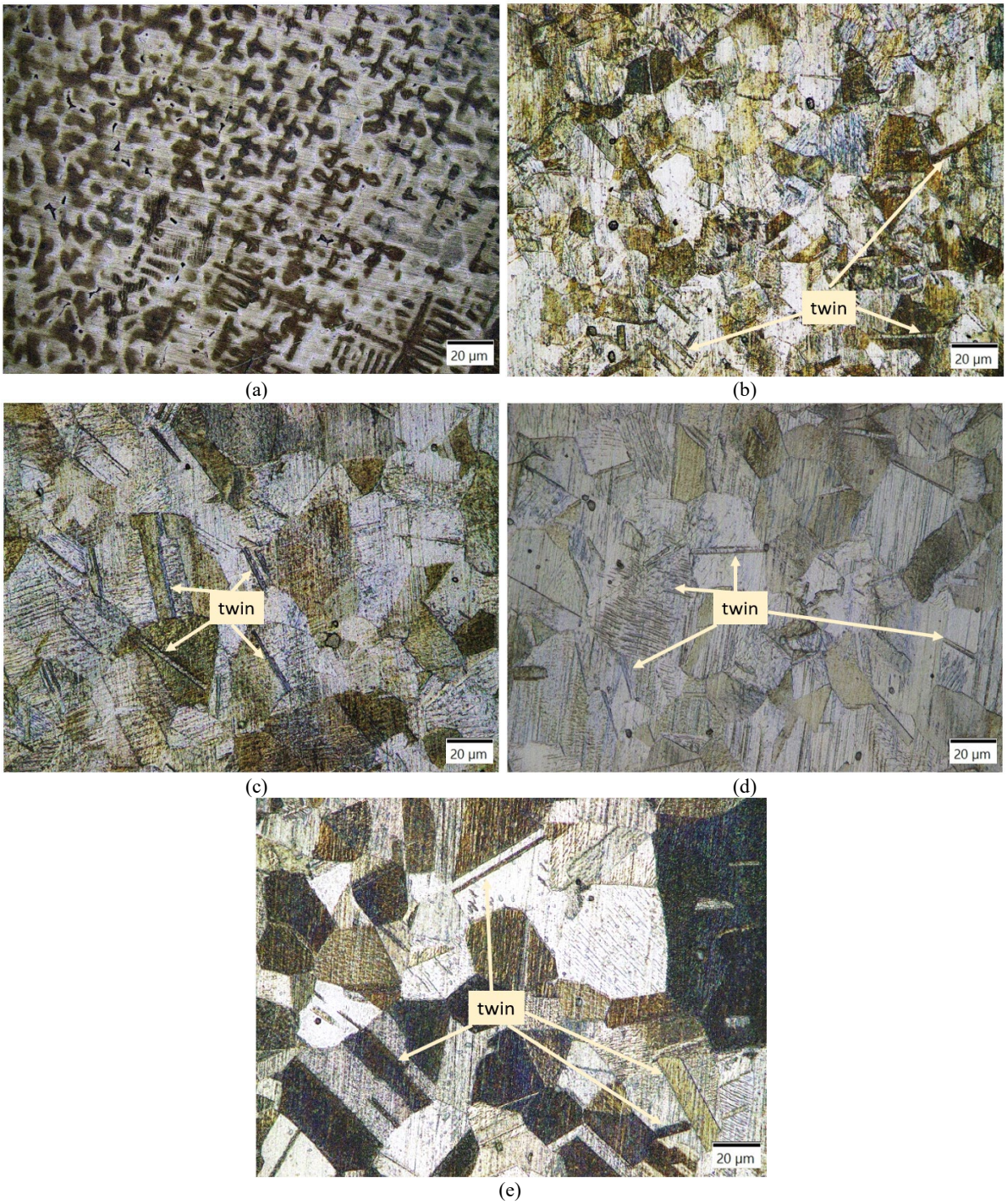

Figure 1. Microstucture of Fe-14Mn-4Si-8Ni-11Cr (a) sample A (as-cast), with hot rolling 900 ℃, (b) sample B (solution treatment 1000 ℃), (c) sample C (solution treatment 1100 ℃), and hot rolling 1000 ℃ (d) sample D (solution treatment 1000 ℃), and (e) sample E (solution treatment 1100 ℃). Etched by Kalling's

The γ -FCC parent phase is depicted in the planes of (111), (200), (220), (311), and (222), which is identical to prior research [14]. The formation of ε-HCP in a small fraction (2.66-6.3%) was assisted by mechanical ground and the shifted temperature transformation (thermal-induced), according to the Clausisu-Clapeyron [10]. There is no significant relationship between rolled or solution temperature and ε-HCP fraction

(Table 3). The higher ε-HCP fraction (6.3%) was obtained by sample D.

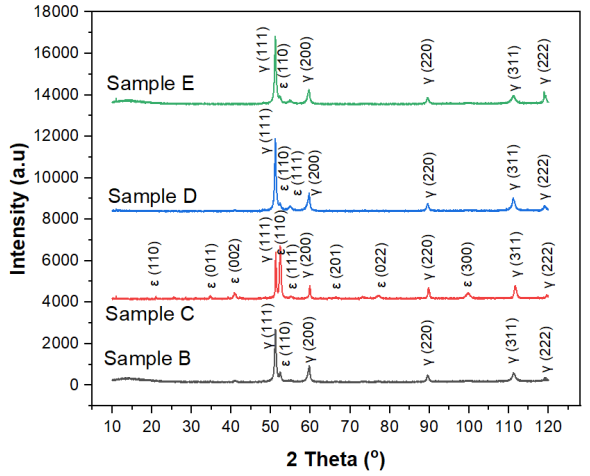

(a)

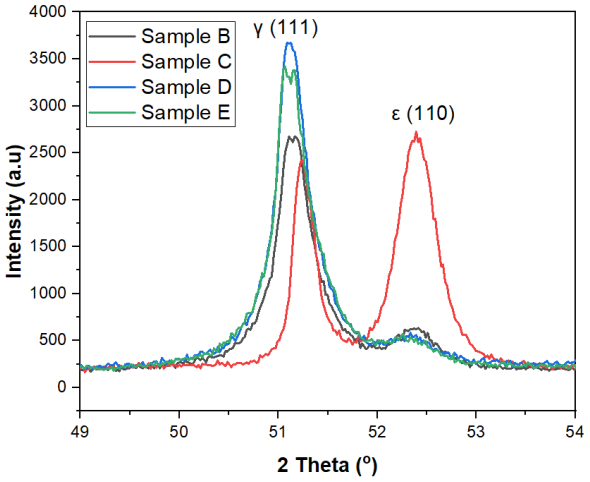

(b)

Figure 2. XRD pattern of (a) Fe-14Mn-4Si-8Ni-11Cr and (b) inserted at 49°-54° of 2θ

Figure 2(b) shows that the reflection peak in 2θ of 51.08° and 52.37° indicated the twin appearance, referring to two symmetric structures in the same layer stuck together in the primary structure (111 γ-phase) [18]. The twin structure reduced the elastic deformation resistance [19]. It is consistent with the microstructure result (Fig. 1). In addition, the lattice parameter of each phase is summarized in Table 3. Lattice a in γ-cell (space group Fm – 3m) is shifted and tend to broaden as the temperature increase, except in sample C. If the lattice parameter is broader, the crystal structure may be less dense, making the material less resistant to mechanical stress [20], and martensitic transformation can quickly occur [19].

3.2 Hardness Analysis

The effect of hot rolling and solution treatment process on Fe-14Mn-4Si-8Ni-11Cr is shown in Fig. 3. The Fe-Mn-Si-Ni-Cr as-cast had the lowest hardness value (175.72 BHN), while sample B had the maximum value (315.48 BHN). The random direction of the dendritic structure most likely caused the low hardness of the as-cast austenitic structure.

Table 3. Lattice paramaters of diffraction pattern in Fe-14Mn-4Si-8Ni-11Cr

Parameter	Sample			
	B	C	D	E
γ-FCC (cubic)				
Space group: Fm – 3m				
Lattice a (nm)	3.59323	3.58506	3.59513	3.59561
Phase fraction	96.24%	93.52%	93.7%	97.34%
E-HCP (hexagonal)				
Space group: P- 3m1				
Lattice a (nm)	4.04652	4.052	4.052	4.0469
Lattice c (nm)	5.09976	5.085	5.085	5.13585
Phase fraction	3.76%	5.648%	6.3%	2.66%
Rwp (%)	3.01	4.4	4.28	4.25
Chi square	1.73	1.970	1.829	1.806

The thermomechanical addition generally improved the hardness value compared to the as-cast sample. Hardness increases are inversely related to the grain size. According to the Hall-Petch equation, the harder the material, the smaller the grain size.

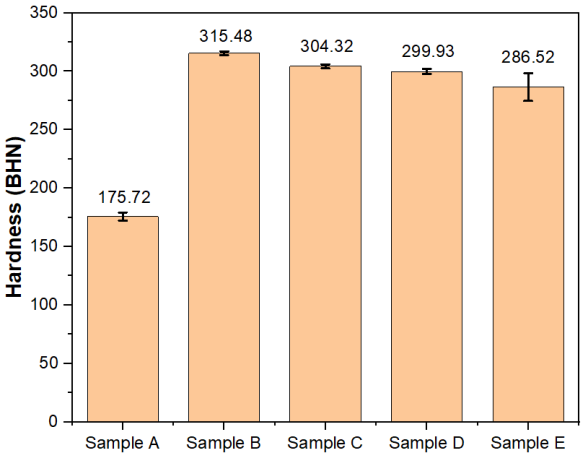

Figure 3. Hardness result of Fe-14Mn-4Si-8Ni-11Cr after hot rolling and solution treatment

The higher temperature in the rolling and solution treatment process provided more activation energy for completing recrystallization and consuming the deformed austenite and its twins, decreasing grain boundary and indirectly lowering hardness [16]. The existence of twins also contributed to the insignificant decrement of hardness in sample C (304.32 BHN) and sample E (286.52 BHN), which increased the work

hardening rate and disturbed dislocation mobility by creating barriers to dislocation glide [21].

3.3 Shape Memory Effect Analysis

The 10% pre-strain and recovery annealing temperature at 600 ℃ were used to determine the SME (in terms of the tensile recovery ratio) based on the microstructure data described above. The SME in Fe-Mn-Si-Ni-Cr shape memory alloys (Fe-SMAs) is derived on the stress-induced ε-martensite transformation (γ(FCC)→ε(HCP)) at room temperature and the reserve transformation (ε → γ) by heating at higher temperature [1]. The effect of thermomechanical conditions on the SME is shown in Fig. 4.

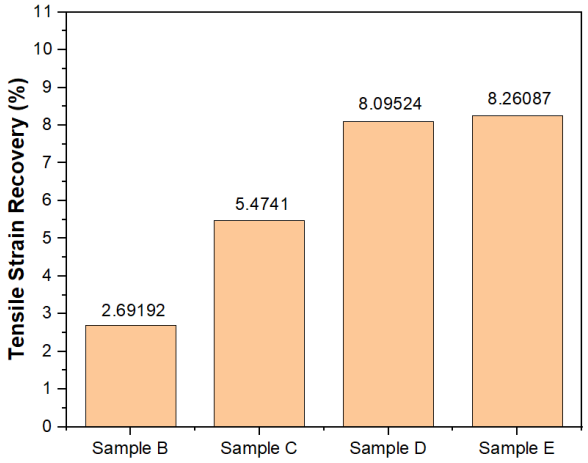

Figure 4. Tensile strain recovery ratio of Fe-14Mn-4Si-8Ni-11Cr

Based on Fig. 4, the tensile recovery ratio of Fe-14Mn-4Si-8Ni-11Cr after annealing at 600℃ is 2.69%, 5.47%, 8.09%, and 8.26% for samples B, C, D, and E, respectively. Compared to other Fe-Mn-Si-Ni-Cr alloys, Fe-14Mn-4Si-8Ni-11Cr shows a relatively good shape memory effect (Table 4). Sample E has the largest recovery strain, around 8.26%, while sample B has the poorest SME (2.69%). The number of SMEs is correlated to the amount of stacking faults, grain size, and the twin's morphology [9]. The larger grain size provided more the atomic arrangement of stacking fault in the FCC austenite during pre-straining can act as a nucleus site for the ε-martensite preferentially nucleated and growth, affecting the improvement of shape memory [9],[14],[22]. The higher temperature in solution treatment significantly promotes the martensite start temperature close to the ambient temperature, generating a high amount of martensite. Choi et al., concluded that the volume fraction of thermally induced ε-martensite after solution treatment increased with the increasing temperature, caused by the reduction of dislocation density along with the increasing grain size, the decreasing critical stress for stress-induced martensite transformation (σ_{SIM}) and the completing recrystallization degree [9].

Table 4. Comparison of SME result of Fe-Mn-Si-Ni-Cr shape memory alloy

Materials	SME	Remark	Ref.
e-14Mn-4Si-8Ni-11Cr	2.69 % – 8.26 %	As hot rolled (900 - 1000 ℃) + solution treated (1000 - 1100 ℃ for 30 minutes)	This study
Fe-21.63Mn-5.6Si-9.32Cr-5.38Ni	4.5 % – 5.5 %	Cold rolling + annealing (1100 - 1150 ℃ for 5-120 minutes)	[15]
Fe-18.54Mn-5.70Si-8.91Cr-4.45Ni	2.7 % – 7.7 %	As-cast, as-annealed (300 – 1100 ℃ for 30 minutes)	[22]

Furthermore, the highest SME in sample E was caused by the lower number of annealing twins, which can't revert through heating in the recovery process [15]. On the other hand, the pre-existing -martensite (Figs.1(b)-1(e)) inhibits the martensite transformation generated by pre-strain because its band intersection acts as a significant barrier to partial dislocation movement.

4. CONCLUSION

The shape memory effect characteristics of Fe-14Mn-4Si-8Ni-11Cr were improved through thermomechanical processing for seismic applications. The austenite became larger as the hot rolling and solution treatment temperature increased, suggesting that recrystallization had been completed and grain growth had occurred for the rolled grain. Because of the lower stacking fault energy and other lead provided the stored energy consumption in the grain boundary, the number of annealing twins increased, the twin spacing became narrower, and the average twin length decreased from 160.88 μm to 90.97 μm at lower rolling and solution treatment temperatures. Furthermore, thermomechanical addition improved the hardness value (286.52-315.48 BHN) compared to the as-cast sample (175.72 BHN). Increasing the hot rolling and solution treatment temperature was found to reduce hardness slightly but noticeably increased the tensile recovery ratio of Fe-14Mn-4Si-8Ni-11Cr. It seemed inversely related to the austenitic grain size, revealing that twin formation as tangles barrier caused the increase in work hardening and disturbed dislocation mobility to gliding. Controlling the grain size of the austenitic phase (29.43-45.57μm) and the pre-existence of ε-

martensite throughout the thermomechanical process resulted in recovery strains varying from 2.69% to 8.26%. The highest-performing SME with an 8.26% tensile recovery ratio was found to be Fe-14Mn-4Si-8Ni-11Cr with the hot rolling and solution treatment at 1100 ℃ temperature.

ACKNOWLEDGMENT

The authors would like to thank financial support from the Research Organization of Nanotechnology and Materials (ORNM-BRIN). This research was conducted using the facilities and technical support at the Research Center for Metallurgy, National Research and Innovation Agency (BRIN).

REFERENCES

[1] J. Mohd Jani, M. Leary, A. Subic, and M. A. Gibson, "A review of shape memory alloy research, applications and opportunities," *Mater. Des.*, vol. 56, no. April, pp. 1078-1113, 2014. Doi: 10.1016/j.matdes.2013.11.084.

[2] A. Tabrizikahou, M. Kuczma, M. L. Plura, E. N. Pursangi, M. Noori, P. Gardoni and S. Li, "Application and modelling of shape-memory alloys for structural vibration control: State-of-the-art review," *Constr. Build. Mater.*, vol. 342, no. PB, pp. 127975, 2022. Doi: 10.1016/j.conbuildmat.2022.127975.

[3] H. Peng, J. Chen, Y. Wang, and Y. Wen, "Key factors achieving large recovery srains in polycrystalline Fe–Mn–Si-based shape memory alloys: A review," *Adv. Eng. Mater.*, vol. 20, no. 3, pp. 1-18, 2018. Doi: 10.1002/adem.201700741.

[4] M. K. El Fawkhry, "The effect of solution treatment temperature on SIEM and shape recovery of Fe-Mn-Si shape memory alloy," *J. Mater. Res. Technol.*, vol. 15, pp. 1069-1075, 2021. Doi: 10.1016/j.jmrt.2021.08.009.

[5] X. Min, T. Sawaguchi, X. Zhang, and K. Tsuzaki, "Reasons for incomplete shape recovery in polycrystalline Fe-Mn-Si shape memory alloys," *Scr. Mater.*, vol. 67, no. 1, pp. 37-40, 2012. Doi: 10.1016/j.scriptamat.2012.03.015.

[6] Y. Yang, C. Leinenbach, and M. Shahverdi, "Simulation and experimental characterization of VC precipitation and recovery stress formation in an FeMnSi-based shape memory alloy," *J. Alloys Compd.*, vol. 940, pp. 168856, 2023. Doi: 10.1016/j.jallcom.2023.168856.

[7] C. Zhang, F. Song, S. Wang, H. Peng, and Y. Wen, "Effect mechanism of Mn contents on shape memory of Fe-Mn-Si-Cr-Ni alloys," *Jinshu Xuebao/Acta Metall. Sin.*, vol. 51, no. 2, pp. 201-208, 2015. Doi: 10.11900/0412.1961.2014.00394.

[8] I. Esquivel, M. F. Giordana, and A. V. Druker, "Effect of heat treatment on the microstructure and shape memory behaviour of Fe-Mn-Si-Ni-Cr alloys," *Mater. Charact.*, vol. 155, pp. 109811, 2019. Doi: 10.1016/j.matchar.2019.109811.

[9] S. Choi, E. Choi, and W. J. Kim, "Austenite grain size effect on recovery stress and recovery strain of Fe-Mn-Si-Cr-Ni-0.01C alloy severely plastically deformed by differential speed rolling," *Mater. Charact.*, vol. 175, pp. 111097, 2021. Doi: 10.1016/j.matchar.2021.111097.

[10] M. Mohri, I. Ferretto, C. Leinenbach, D. Kim, D. G. Lignos, and E. Ghafoori, "Effect of thermomechanical treatment and microstructure on pseudo-elastic behavior of Fe-Mn-Si-Cr-Ni-(V, C) shape memory alloy," *Mater. Sci. Eng. A*, vol. 855, pp. 143917, 2022. Doi: 10.1016/j.msea.2022.143917.

[11] H. Peng, Y. Wen, Y. Du, Q. Yu, and Q. Yang, "Effect of manganese on microstructures and solidification modes of cast Fe-Mn-Si-Cr-Ni shape memory alloys," *Metall. Mater. Trans. B Process Metall. Mater. Process. Sci.*, vol. 44, no. 5, pp. 1137-1143, 2013. Doi: 10.1007/s11663-013-9880-2.

[12] O. Matsumura, T. Sumi, N. Tamura, K. Sakao, T. Furukawa, and H. Otsuka, "Pseudoelasticity in an Fe-28Mn-6Si-5Cr shape memory alloy," *Mater. Sci. Eng. A*, vol. 279, no. 1-2, pp. 201-206, 2000. Doi: 10.1016/s0921-5093(99)00644-9.

[13] S. Y. Jiang, Y. Wang, X. D. Xing, and Y. Q. Zhang, "Stress-induced martensite phase transformation of FeMnSiCrNi shape memory alloy subjected to mechanical vibrating polishing," *Trans. Nonferrous Met. Soc. China (English Ed.*, vol. 30, no. 6, pp. 1582-1593, 2020. Doi: 10.1016/S1003-6326(20)65321-3.

[14] M. M. Pan, X. M. Zhang, D. Zhou, R. D. K. Misra, and P. Chen, "Fe-Mn-Si-Cr-Ni based shape memory alloy: Thermal and stress-induced martensite," *Mater. Sci. Eng. A*, vol. 797, pp. 140107, 2020. Doi: 10.1016/j.msea.2020.140107.

[15] L. Yong, Q. Luo, H. Peng, J. Yan, B. Xu,

and Y. Wen, "Dependence of shape memory effect on austenitic grain sizes in thermo-mechanical treated Fe-Mn-Si-Cr-Ni shape memory alloys," *Mater. Charact.*, vol. 169, pp. 110650, 2020. Doi: 10.1016/j.matchar.2020.110650.

[16] N. Bozzolo and M. Bernacki, "Viewpoint on the formation and evolution of annealing twins during thermomechanical processing of FCC metals and alloys," *Metall. Mater. Trans. A Phys. Metall. Mater. Sci.*, vol. 51, no. 6, pp. 2665-2684, 2020. Doi: 10.1007/s11661-020-05772-7.

[17] K. W. Park, E. Choi, and W. J. Kim, "Grain size effect on the recovery stress and strain of a Fe–Mn–Si shape memory alloy in a wide range of grain sizes," *Mater. Sci. Eng. A*, vol. 856, pp. 143947, 2022. Doi: 10.1016/j.msea.2022.143947.

[18] Y. Chen, A. Li, Z. Ma, G. Kang, D. Jiang, K. Zhao, Y. Ren, L. Cui, K. Yu, "Revealing the mode and strain of reversible twinning in B19′ martensite by in situ synchrotron x-ray diffraction," *Acta Mater.*, vol. 236, p. 118131, 2022. Doi: 10.1016/j.actamat.2022.118131.

[19] P. Chowdhury, "Frontiers of theoretical research on shape memory alloys: A general overview," *Shape Mem. Superelasticity*, vol. 4, no. 1, pp. 26-40, 2018. Doi: 10.1007/s40830-018-0161-4.

[20] L. La Rosa and F. Maresca, "On the impact of lattice parameter accuracy of atomistic simulations on the microstructure of Ni-Ti shape memory alloys," *Model. Simul. Mater. Sci. Eng.*, vol. 30, no. 1, 2022. Doi: 10.1088/1361-651X/ac3b9e.

[21] K. Renard and P. J. Jacques, "On the relationship between work hardening and twinning rate in TWIP steels," *Mater. Sci. Eng. A*, vol. 542, pp. 8-14, 2012. Doi: 10.1016/j.msea.2012.01.123.

[22] H. Peng, L. Yong, S. Wang, and Y. Wen, "Role of annealing in improving shape memory effect of as-cast Fe-Mn-Si-Cr-Ni shape memory alloys," *Metall. Mater. Trans. A Phys. Metall. Mater. Sci.*, vol. 50, no. 7, pp. 3070-3079, 2019. Doi: 10.1007/s11661-019-05233-w.

Metalurgi (2023) 2: 65 - 72

METALURGI
Majalah Ilmu dan Teknologi
p-ISSN 0126-3188 | e-ISSN 2443-3926
ejurnalmaterialmetalurgi.lipi.go.id

THE EFFECT OF Al_2O_3 AND STIRRING TIME ON DENSITY AND POROSITY OF ALUMINUM ADC12 FOAM

Yeni Muriani Zulaida*, Muhammad Nurul Izzudin, Suryana
Department of Metallurgy, Sultan Ageng Tirtayasa University
Jl. Jenderal Sudirman Km 3, Cilegon, Banten, Indonesia 42435
*E-mail: yeni_m_zulaida@untirta.ac.id

Received: 11-03-2023, Revised: 07-08-2023, Accepted: 15-08-2023

Abstract

The instability of the foam forming during metallic foam manufacture commonly occurs, which will cause undesirable pores. The stability of the foam structure is one of the important factors. A stabilizer can maintain the foam cell during the melting process. In this study, the metal used is ADC12 with a 12 wt.% of Si element content, and the foaming agent is $CaCO_3$. $CaCO_3$ will produce gas to form bubbles in the melt during the solidification process and use a stabilizer to strengthen cell walls so that foam does not easily fall off or collapse. The stabilizer uses Al_2O_3 with the variation of Al_2O_3 are 1 to 3 wt.%. The stirring time is as variable as well. A stirring process is conducted to distribute foaming agents so that the foam distribution is more homogeny throughout the aluminum foam. The variation of the stirring time is carried out for 60, 120, and 180 seconds. The results show that as the time of stirring and the addition of stabilizer increases, the porosity will rise, but the density decrease. Compressive strength results show it has no significant relation with increasing the stabilizer and stirring time. The highest compressive strength is obtained in the sample with a stirring time of 120 seconds with an Al_2O_3 content of 1 wt.%.

Keywords: *ADC 12 metal foam, foaming agent, stirring, Al_2O_3*

1. INTRODUCTION

The popularity of aluminum foam nowadays has increased. It can be investigated easily by the number of scientific articles that discuss it [1]. Metal foams are known for their unique combinations of physical and mechanical properties, such as lightweight, higher specific strength & stiffness, improved elevated temperature strength, and excellent energy absorption capacity at very low plateau stress. The implementation of aluminum foam in the automotive and aerospace fields is unquestionable. Aluminum foam can be used as crash energy or vibration-absorbing material [2]. Because of its lightweight material, aluminum foam can reduce the weight of vehicles. Mass-reduction vehicles achieve significant weight loss, reduce greenhouse gas emissions, and save intake fuel [3]. All of these are the advantages of using metal foam.

Different methods have been developed to produce foams, which can be divided into two categories: direct foaming by introducing gas bubbles into a conditioned melt [4] and foaming with the help of blowing agents [5]. Metal foam making using the molten metal can be called the direct method because liquid metal can form foam by directly injecting gas or gas from blowing agents [6]. Gas that appears in molten metal will form gas bubbles and be dispersed in the liquid. Generally, gas bubbles formed in molten metal tend to immediately rise to the surface due to the high buoyancy forces in the high-density melt. However, this upward movement will be hampered by increasing the viscosity of the liquid metal. This condition can be conducted by adding fine ceramic powders or alloying elements to form stable melt particles [7].

Using foaming agent $CaCO_3$ can produce foam under optimum conditions, resulting in a

DOI : 10.55981/metalurgi.2023.707

Metalurgi is Sinta 2 Journal (https://sinta.ristekbrin.go.id/journals/detail?id=3708) accredited by Ministry of Research & Technology, Republic Indonesia

density of 0.9 g/cm^3 with a rounded pore shape. [8]. Too high a stirring speed, up to 2000 rpm, causes the porosity to increase, but the pore size decreases. The use of $CaCO_3$ is considered very efficient and effective and thus can replace the role of conventional TiH_2 foaming agents [9]. The effect of porosity percentage is very significant on the compressive strength of the aluminum foam. The value of the porosity is higher; the foam strength will be low [10].

In a previous study, aluminum in the liquid will react to form aluminum oxide (Al_2O_3) and then continue with calcium carbide to become calcium-alumina [11]. It will increase the viscosity of the melt so that the bubbles that form do not quickly come out to the surface. In this study, the formed aluminum oxide slag was cleaned, so how effective the addition of Al_2O_3 in forming porosity in the foam metal.

So, this study aims to understand the effect of additional alumina and stirring time on the density and porosity of foam aluminum, pore shape and size, and the strength of the aluminum foam as a foaming agent using calcium carbonate ($CaCO_3$).

2. MATERIALS AND METHODS

This experiment uses base metal aluminum ADC12 and foaming agent calcium carbonate, as much as 300-gram dan 2 wt.%. The liquid metal stabilizer compound uses alumina (Al_2O_3) with a composition variation of 1, 2 and 3 wt%. All materials melt in an electric furnace. Each specimen was coded based on the stirring time and stabilizer composition, as described in Table 1. S denotes the sample, the first two or three numbers indicate the stirring time, and the last digit indicates the alumina composition. For example, if the specification is S1203, the stirring is carried out for 120 minutes with a 3 wt.% alumina composition.

First, the aluminum ingot was cut into smaller sizes and then put into an electric furnace until around 800 °C. After the metal has melted, the slag on the surface of the liquid is cleaned and then mixed with alumina and stirred with stirring variations of 60, 120, and 180 seconds with a constant rotational speed of 1200 rpm. The stirring process at a set time aims to obtain an evenly distributed alumina in the melt, then the foaming agent $CaCO_3$ is added, stirred for 60 seconds, and held for 3 minutes.

At a temperature of 800 °C, $CaCO_3$ has decomposed into CaO and CO_2. CO_2 gas will be trapped in melted molten aluminum and form bubbles in large quantities and will eventually be referred to as foam. The alumina slag that comes from the reaction of melted aluminum with the surrounding air is removed from the melt surface. It aims to observe the effect of the added alumina more clearly. It is different from what was done by previous researchers who used alumina that came from the reaction between the melt and air [11]. Then, the same process was carried out for other research variations of the alumina composition.

Density and porosity can be calculated using Archimedes' principle [12]. Density (ρ_{sample}) and porosity tests were carried out to determine the percent pore level formed. In the density test, the sample is weighed to determine the dry sample weight (M_k). Then, the sample is immersed in a container filled with water for 1 hour and weighed to determine the wet sample weight (M_b). Then, do the calculations using equation (1) after knowing the value of the hanging mass (W_t), the sample mass in water (W_b), and the specific gravity of water (ρ_{water}) :

$$\rho_{sample} = \frac{M_k}{M_b-(W_b-W_t)} \times \rho_{air} \quad \text{.....(1)}$$

Porosity percentage can calculate using this equation follow,

$$Porosity = 1 - \left(\frac{\rho_{Aluminum}}{\rho_{foam}} \times 100\%\right) \text{....(2)}$$

Compressive strength is observed to obtain the ability of metal foam to accept loads. Compressive testing of aluminum foam uses a universal testing machine Shimadzu AG-X Plus. The 10 KN of load and 2.5 mm/minute of loading speed. The dimension of the compressive test sample is 20x20x30 mm according to the standard. Mechanical properties of commercial aluminum metal foam according to reference in the 0.04-14 MPa [13]. Compressive strength was measured by going through a compressive test with a test speed of 2.5 mm/min at a temperature of 21.2 °C with a humidity of 52.9% RH.

Figure 1. Aluminum without adition foaming agent

The next step is to observe the pore morphology of foam aluminum. This observation includes the pore size and pore area fraction. This step is supported by the ImageJ application to obtain the values. The pore size is determined by measuring the pores' length and width and then averaged.

3. RESULT AND DISCUSSION

After adding the foaming agent and stabilizer, the dimension of the casting is higher than before, which shows that the pore is formed in the melt during solidification. It is possible to see the differences between the sample before and after foaming after cutting it in the transversal direction. The sample has no apparent porous structure without adding the foaming agent and stabilizer (Fig. 1).

The effect of the foaming process is that the casting colour is darker than the casting without the process. After the tranverse cut, the surface have porous (Fig. 2). The composition of Al_2O_3 influences the morphology, density, porosity and, compressive strength of the aluminum foam.

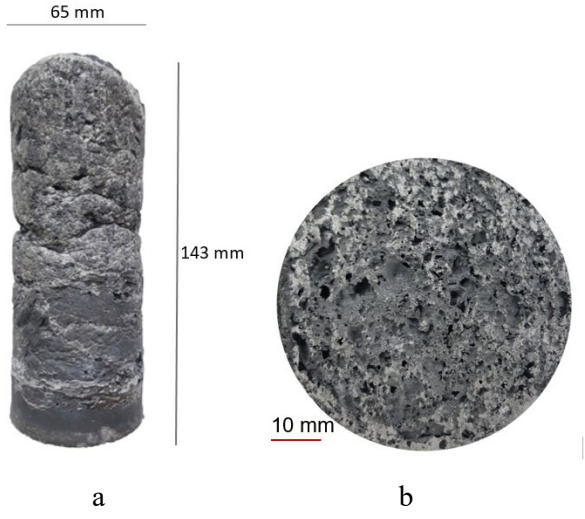

Figure 2. (a) Specimen as cast before cutting, (b) aluminum with adition foaming agent

3.1 Morphology

Figure 3 shows that all samples form pores. The change in the morphology of this precursor material into foam was due to the addition of partition materials that have their respective purposes, namely $CaCO_3$ as a foaming agent and Al_2O_3 as a foam stabilizer.

From the data shown in Table 1, it can be observed that there are differences in the size and fraction of the pore area in the sample cut layers. The S1201 specimen has the highest average pore size and the lowest pore area fraction. The sample with a longer stirring time of 180 seconds will produce a smaller pore size than others, with a larger pore area fraction. These differences will affect the percentages of porosity, density values, compressive strength, and energy present in each sample.

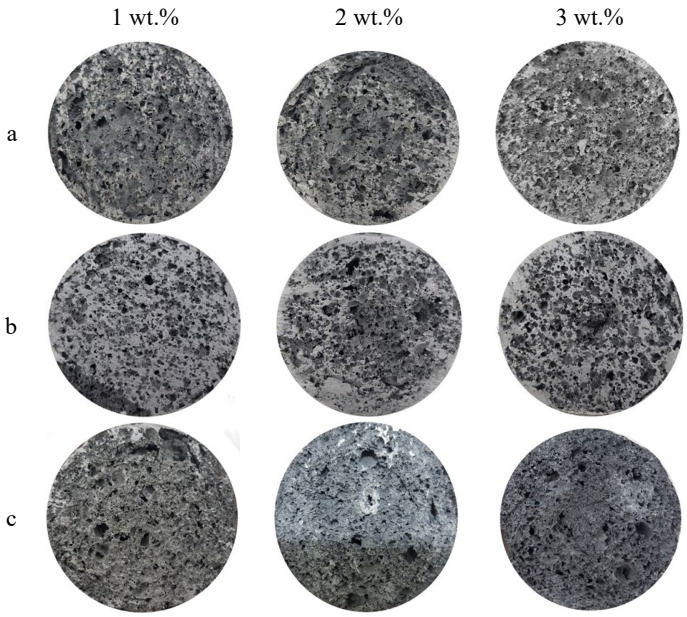

Figure 3. Pore at each stirring time (second) (a) 60, (b) 120, (c) 180

The pore shape can be seen in Fig. 4. The alumina composition affects the pore wall thickness. The specimens with the same stirring time, namely 120 seconds for 2 wt% by weight (S1202) alumina, had thinner walls and more irregular foam shapes than samples with 1 wt.% of alumina composition.

Table 1. Pores size and fraction in every specimen

No	Specimens	Pore Size average (mm)	Pore Fraction Area (%)
1	S601*	1.85	54.52
2	S602	1.72	50.62
3	S603	1.39	50.96
4	S1201	2.46	38.66
5	S1202	1.68	56.06
6	S1203	2.2	54.20
7	S1801	0.94	71.64
8	S1802	0.95	75.84
9	S1803	1.02	76.29

Note : *S is specimen, 60 is stirring time, 1 is stabilizer content

3.2 Density and Porosity

Figure 5 shows the effect of alumina content on the density and porosity of aluminum foam. The blue curve shows 60 seconds of stirring, red for 120 seconds, and green for 180 seconds of stirring.

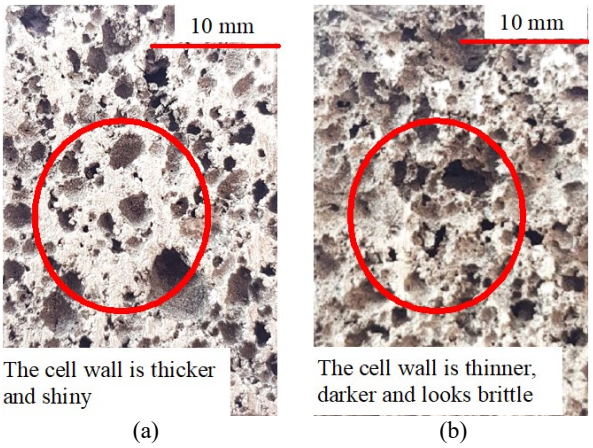

Figure 4. The differences in the pore wall thickness at stirring time 120 seconds with different compositions of alumina (wt.%) (a) 1, and (b) 2

The highest porosity was obtained in 2 wt.% of the alumina composition with a stirring time 120 seconds while adding 3 wt.% of alumina at stirring time 120 seconds which results in lower porosity than the addition of 2 wt.% of alumina. This exhibits that the additives added to the aluminum melt have yet to shown that increasing the levels of additives that increase porosity and reduce density.

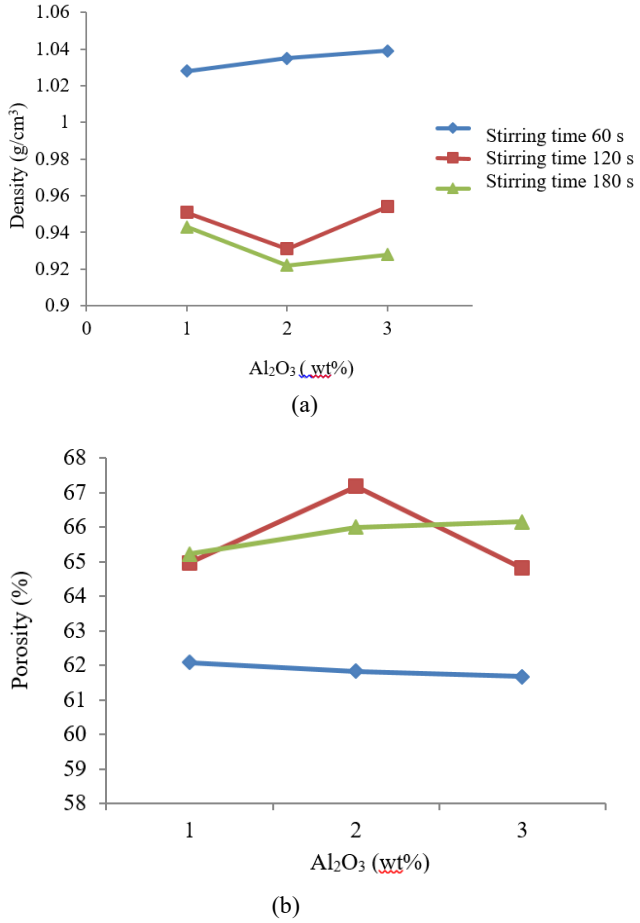

Figure 5. The effect of alumina composition on (a) the density, and (b) the porosity value

Different things are shown in the effect of increasing the stirring time. In Figure 6, the blue, red, and green lines indicate the alumina composition of 1, 2, and 3 wt.% consecutively. The curves show that increasing the stirring time can increase the porosity and decrease the density. It is due to the effect of the stirring process that can help distribute the foaming agents and additives more evenly in the aluminum liquid.

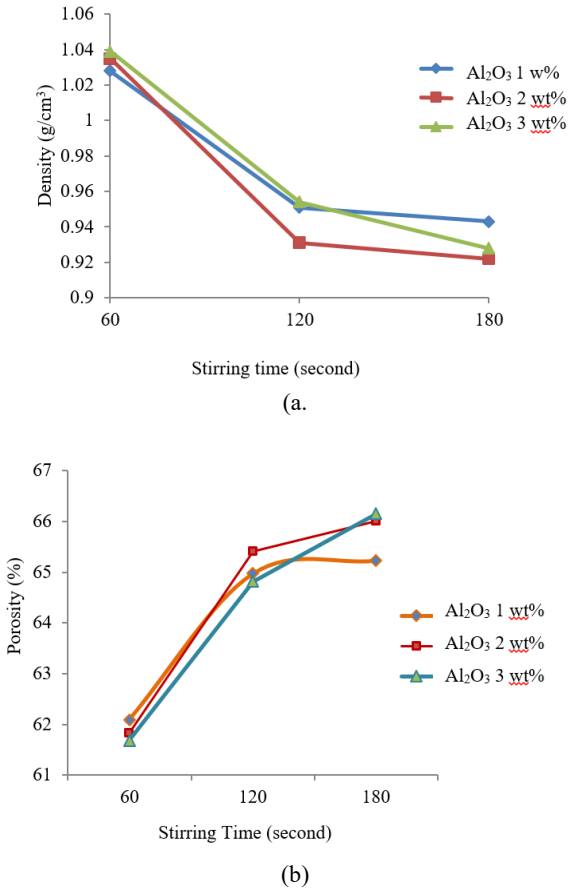

Figure 6. The effect of stirring time on (a) the density and (b) the porosity value

In the 3 wt.% alumina composition, from the results of successive stirring for 60, 120, and 180 seconds, the density values obtained were 1.039, 0.954, and 0.928 gr/cm^3 consecutively, while for porosity were 61.68%, 64.82%, and 66.15%. According to the graphic trend, the same direction can be seen in other alumina compositions.

3.3 Compresive Strength of Aluminum Foam

The effect of adding Al_2O_3 on the compressive strength produced from all aluminum foam specimens can be seen in the figure presented in Fig. 7. The change of the compressive strength values for each sample as the effect of the Al_2O_3 content increases.

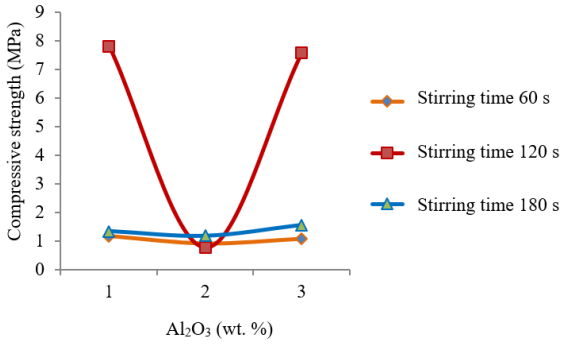

Figure 7. The effect of addition Al_2O_3 on compressive strength of aluminum foam

The compressive strength values obtained from all samples increased with each difference in stirring time. During the 60-second mixing time marked with the orange line, there was an increase and decrease in the compressive strength from 1.17 MPa to 0.90 Mpa, and then it increased again to 1.07 MPa. A significant difference in compressive strength values was obtained for a specimen with a stirring time of 120 seconds marked with a red line. The difference in the compressive strength value in sample 4 was 7.82 MPa, and it decreased very significantly to 0.76 MPa then experienced a significant increase again to 7.58 Mpa.

Figures 8 and 9 show the difference in the pressure test curve lines. Those lines tend to be smooth and go up and down. This indicates that there are differences in the mechanical properties of the samples themselves and that they can be classified into ductile or brittle samples. In the pressure test results, the specimen with a stirring time of 120 seconds had the highest pressure test value compared to other conditions, around 70.73 joules. Meanwhile, the non-smooth curve, as shown in the S1202 sample, includes samples with brittle properties, and you can also see that the energy value is the lowest compared to the other samples, namely 9.58 joules. The shape of the curve that goes up and down is because when pressing is done, the pore walls are immediately destroyed, and consequently, the pressure value at a certain point on the curve decreases. This is also described in previous research [14].

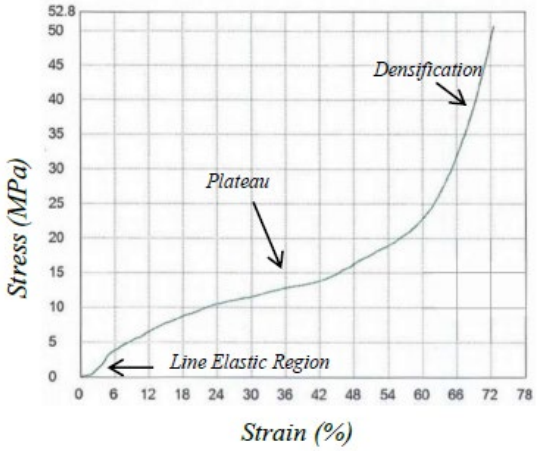

Figure 8. Compressive test result at 120 seconds of stirring time with addition Al_2O_3 1 wt% (S1201)

Representative stress-strain curve from sample S1202 during compression testing (Fig. 8). The first zone is the linear elastic at strain values up to 3% or 4%. In this first zone, the pore shape has not changed permanently. The second zone is the plateau zone, which continues with strain values up to around 6-70%. Plateau is a state of little or no change following a period of activity or progress, but in this case, the stress continues to move up even though it is slower than the first zone. As the pressure increases in this zone, the pores begin to collapse and continue to collapse until the pores are flatter and have the properties of solid materials.

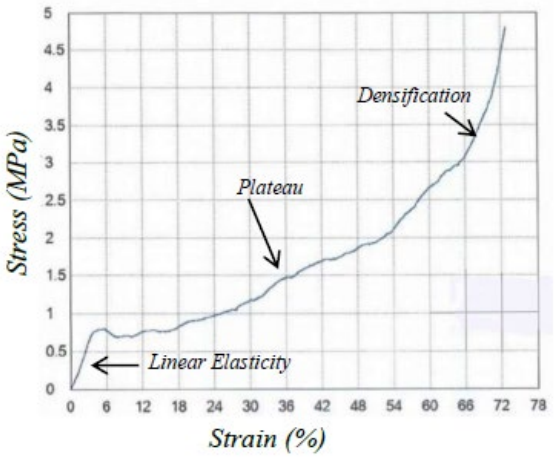

Figure 9. Compressive test result at 120 second of stirring time with addition Al_2O_3 2 wt.% (S1202)

The third zone is the densification zone, with a strain value of around 70% and above. In this zone, the pore wall and the opposite wall close together until they touch each other, and the pore completely collapses, indicated by a significantly increased stress value.

4. CONCLUSION

In this research, adding alumina aims to increase the viscosity of the aluminum melt so that the bubbles that form do not easily come out of the melted surface. Stirring ensures that the alumina and calcium carbonate are distributed evenly throughout the liquid. The conclusions of this study are as follows: The addition of alumina to aluminum melt has not shown a significant effect on density and porosity in the formation of foam. This is obtained value being still lower than the metal foam criteria.

Stirring time shows a significant effect on foam formation. This can be seen by decreasing the density value and increasing the porosity value. This could be due to the foaming agent $CaCO_3$ and additive Al_20_3, which are more evenly distributed in the aluminum alloy.

The distribution of pores formed in the samples improved with increasing stirring time, even though the larger the pores became, the longer the stirring. The higher the compressive strength value of aluminum foam, the longer the stirring time with the addition of Al_2O_3.

ACKNOWLEDGMENT

The authors would like to thank and appreciate to all parties involved, Metallurgy Laboratory of Metallurgical Department, Engineering Faculty, University of Sultan Ageng Tirtayasa for all their scientific discussion and technical support during aluminum foam experiment.

REFERENCES

[1] F. Garai, "Modern applications of aluminium foams," *Int. J. Eng. Manag. Sci.*, vol. 5, no. 2, pp. 14-21, 2020. Doi: https://doi.org/10.21791/ijems.2020.2.3.

[2] S. S. Sharma, S. Yadav, A. Joshi, A. Goyal, and R. Khatri, "Application of metallic foam in vehicle structure: A review," *Mater. Today Proc.*, vol. 63, pp. 347-353, 2022. Doi: 10.1016/j.matpr.2022.03.201.

[3] A. Kumar, R. Maithani, A. Kumar, D. Kumar, and S. Sharma, "An all-aluminium vehicle's design and feasibility analysis," *Mater. Today Proc.*, vol. 64, pp. 1244-1249, 2022. Doi: 10.1016/j.matpr.2022.03.714.

[4] J. Banhart and J. Baumeister, "Production methods for metallic foams," *Mater. Res. Soc. Symp. - Proc.*, vol. 521, pp. 121-132, 1998. Doi: 10.1557/proc-521-121.

[5] T. Miyoshi, M. Itoh, S. Akiyama, and A. Kitahara, "ALPORAS aluminum foam: Production process, properties, and applications," *Adv. Eng. Mater.*, vol. 2, no. 4, pp. 179-183, 2000. Doi: 10.1002/(SICI)15272648(200004)2:4<179::AID-ADEM179>3.0.CO;2-G.

[6] J. Banhart, "Manufacture, characterisation and application of cellular metals and metal foams," *Prog. Mater. Sci.*, vol. 46, no. 6, pp. 559-632, 2001. Doi: 10.1016/S0079-6425(00)00002-5.

[7] J. Banhart, "Metal foams: Production and stability," *Adv. Eng. Mater.*, vol. 8, no. 9, pp. 781-794, 2006. Doi: 10.1002/adem.200600071.

[8] A. M. Solhi, J. K. Allafi, M. Yusefi, M. Yazdani, and A. Mohammadzadeh, "Fabrication of aluminum foam by using $CaCO_3$ foaming agent," *Material Research Express*, pp. 11-14, 2018. DOI: 10.1088/2053-1591/aad88a.

[9] T. Nakamura, S. V. Gnyloskurenko, K. Sakamoto, A. V. Byakova, and R. Ishikawa, "Development of new foaming agent for metal foam," *Mater. Trans.*, vol. 43, no. 5, pp. 1191-1196, 2002. Doi: 10.2320/matertrans.43.1191.

[10] D. S. P. Nugroho, A. W. Nugroho, and B. N. Rahman, "Pengaruh penambahan blowing agent $CaCO_3$ terhadap porositas dan kekuatan tekan aluminium foam dengan cara melt route process," *Tek. Mesin UMY*, pp. 1-6, 2012.

[11] A. A. K. Sutarno, and S. Soepriyanto, "Pengaruh kalsia alumina (CaO. Al_2O_3) pada busa aluminium AL-7000 dengan agen pembusa kalsium karbonat ($CaCO_3$)," *Pros. Simp. Nas. Inov. dan Pembelajaran Sains 2015*, vol. 2015, pp. 149-152, 2015.

[12] ASTM, "ASTM C373-88 standard test method for water absorption, bulk density, apparent porosity, and apparent specific gravity of fired whiteware products," *Astm C373-88*, vol. 88, pp. 1-2, 1999.

[13] M. F. Ashby, A. Evans, N. A. Fleck, L. J. Gibson, J. W. Hutchinson, H. N. G. Wadley, and F. Delale, "Metal foams : A design guide, *Appl. Mech. Rev.*, vol. 54, no. 6, pp. B105-B106, 2000. Doi:10.1115/1.1421119.

[14] D. C. Curran, "Aluminium foam production using calcium carbonate as a foaming agent," University of

Cambridge, 2003. [Online]. Available: https://www.repository.cam.ac.uk/handle/1810/252945. (accessed July 03, 2023)

Metalurgi (2023) 2: 73 - 82

METALURGI
Majalah Ilmu dan Teknologi
p-ISSN 0126-3188 | e-ISSN 2443-3926
ejurnalmaterialmetalurgi.lipi.go.id

EFFECT OF COOLING-MEDIUM INDUCED INITIAL STRUCTURE BEFORE INTERCRITICAL ANNEALING ON THE MICROSTRUCTURE AND MECHANICAL PROPERTIES OF LOW ALLOY DUAL-PHASE STEEL

Toni Bambang Romijarso[a,b*], Miftakhur Rohmah[a], Myrna Ariati[b], Efendi Mabruri[a], and Eddy Sumarno Siradj[b]

[a] Research Center for Metallurgy, National Research and Innovation Agency
Management Building 720, B.J. Habibie Sains and Technology Area, Banten, Indonesia 15314
[b]Department of Metallurgy and Materials Engineering, Universitas Indonesia
UI Campus, Kukusan, Depok, Jawa Barat, Indonesia 16425
*E-mail: toni001@brin.go.id

Received: 13-07-2023, Revised: 31-08-2023, Accepted: 11-09-2023

Abstract

The present research focused on determining the effect of cooling-medium-induced initial structure before the intercritical annealing induced dual-phase structure in the low alloy steel. Low carbon steel, which consists of containing 0.09 wt.% C was heated at 920 °C for 30 minutes to austenitization and then cooled in various media to provide the different initial structures before the IA (intercritical annealing) process. After austenization, the cooling process in the furnace and open-air provided a ferrite-pearlite phase, while the cooling process in water generated full martensite as the initial structure. Afterwards, the sample was intercritical-annealed at 750 °C (temperature between Ac1 and Ac3 lines or intercritical zone) for 10 minutes and then quenched in water. The water quenching after the austenitizing process improved the mechanical strength of steel (919 MPa), compared to the as-received state (519 MPa) due to martensite formation. As the cooling rate increased after the austenitizing process, the tensile strength increased and the elongation decreased. The different structures before intercritical annealing affected the martensite volume fraction and further correlated with improving mechanical properties. The ferrite and pearlite, as the initial structure before the IA process, provide a smaller fraction of martensite (18.36 vol.% for furnace cooling and 27.85 vol.% for open-air cooling). In contrast, the full martensite as the initial structure before IA generates a higher fraction of martensite (39.25 vol.%). The tensile strengths obtained were 512, 516, and 541 MPa with elongations of 29.8%, 30.1% and 32.6% for cooling furnace, open air and water, respectively. The strain-hardening behavior during the intercritical annealing is not affected by the initial process of the structure.

Keywords: *Dual-phase steel, intercritical anealing, low-alloy carbon steel, fraction of martensite*

1. INTRODUCTION

Dual-phase steel provides a superior mix of strength and ductility, more excellent weldability, an outstanding balance of strength and formability, and relatively easy processing methods due to its microstructure consisting of a matrix of ferrite and martensite/bainite phases. It has been widely utilized in the automobile industry, mainly passenger cars, since its development in 1970 [1]-[3]. When applied to vehicles, dual-phase steel was believed to reduce vehicles' weight and reduce exhaust emissions [4].

There are three primary methods for manufacturing DP (dual phase) steel: (1) direct intercritical heat treatment followed by water quenching (intercritical heat treatment-IHT), (2) austenitization and cooling into an intercritical

DOI : 10.55981/metalurgi.2023.727

Metalurgi is Sinta 2 Journal (https://sinta.ristekbrin.go.id/journals/detail?id=3708) accredited by Ministry of Research & Technology, Republic Indonesia

temperature zone followed by water quenching (continuous IHT), and (3) intercritical annealed of the quenched martensitic structure followed by water quench (IQ route) [4]. However, because of the varied initial microstructure formation, the morphological characteristics (including martensitic distribution, volume fraction, and grain size) of DP steel might be highly diverse.

Several previous researchers have studied the effect of initial microstructure on the mechanical properties of DP steel. The martensite and ferrite morphology can respond to the work hardening capacity, which improves mechanical properties [1]. Kalhor et al., [5] confirmed that the different initial microstructures significantly affect lath martensite distribution, mechanical properties (resulting in ~800 MPa), and fracture features of the 0.18C-0.14Si-1.29Mn steel. Jamei et al., [6] concluded that the rapid cooling before intercritical annealing on the 0.035C-0.268Mn-0.035Si steel provided a lower ratio between ultimate tensile strength and yield strength (UTS/YS) than the slow cooling.

Adamczyk's research (0.09C- 1.50Mn-0.014P-0.009S) found that the initial structure affects the martensite morphology in the dual-phase structure obtained [7]. But, the refined martensite island ~4.5 µm, which resulted from water quenched IHT process, enhanced the tensile strength and work hardening capacity. Contrarily, the refining grain with globular morphology was observed to improve the tensile strength without sacrificing ductility [1]. Besides that, the austenite distribution has significantly affected the morphology of the recrystallized ferrite grain and martensite evolution [8]. However, limited literature is reported to investigate the correlation of structure morphology on DP steel's mechanical and strain-hardening behavior. Besides controlling the heat treatment process, the carbon level on the austenitic phase also affected the martensite transformation behavior due to the changes in martensite start (Ms)temperature [9].

However, the intercritical annealing process of low-alloy steels has not been thoroughly studied. Adjusting the temperature and cooling rate after austenitization can control the initial structure's characteristics before intercritical annealling. Based on the previous research, the different cooling rate was provided by variations in cooling media. So, the focused present study evaluates the effect of the cooling-medium-induced initial structure after the austenitization on the microstructure transformation and its correlation with mechanical properties of low alloy steel when subjected to intercritical annealing.

2. MATERIALS AND METHODS

A low-alloy carbon steel sheet as-received with dimensions of 220 x 20 x 3 mm (length x width x thickness) was used in this study, which has the chemical composition presented in Table 1.

Table 1. Chemical composition of as-received low-alloy carbon steel (wt.%)

C	Si	Cr	Mn	Ni
0.0948	0.3651	0.5548	0.5839	0.0744
P	**S**	**Cu**	**Mo**	**V**
0.0064	0.0033	0.2445	0.0009	0.0004

The schematic of the dual-phase heat treatment process in the present study is displayed in Figure 1. Six samples were austenitized at 920 °C for 30 minutes to provide a full austenite structure. To generate a different initial microstructure before intercritical annealing, each sample was cooled at a different cooling rate using furnace cooling (annealed state), open-air cooling (normalizing), and water quenching. Afterward, the sample was re-heated to an intercritical annealing temperature (~750 °C) for 10 minutes to transform the dual-phase structure. This temperature was estimated in two zone (α+γ phase) by calculating the A_{c1} and A_{c3}, according to Haugardi Equation [9]-[10]:

$$A_{C1}(°C)=739-22C-7Mn+2Si+14Cr+13Mo-13Ni \quad (1)$$

$$A_{C3}(°C)=902-225C-11Mn-19Si-5Cr+13Mo-20Ni+55V \quad (2)$$

Based on Eq. 1-2 and chemical composition, the estimated A_{c1} and A_{c3} were 740 °C and 863 °C, respectively. Besides that, this steel's Ms (martensite start) can be calculated using the KE Thelning Equation, following Eq. 3 [10]. The result of the calculation of Ms is 486 °C.

$$Ms(°C) = 561-474C-33Mn-17Ni-17Cr-21Mo \quad (3)$$

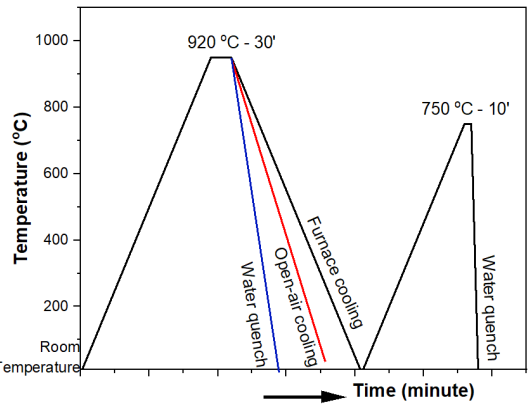

Figure 1. Schematic diagram of heat treatment process performed in this work

The metallographic observation was conducted to analyze the microstructure evolution during intercritical annealing. All samples were wet-ground by SiC paper with a roughness of 80 to 2000 grit. Then, sample was polished using a slurry of alumina powder (5, 3, 1, and 0.5 μm) to obtain the mirror-like surface. After that, the sample was etched into a 2% nitric acid solution (2% Nital). The metallographic test used an optical microscope (Olympus BX53M) and scanning electron microscope (JEOL JSM 639OA) for higher magnification. The grain size was calculated by Intercept method, according to ASTM E-112 [11]. GSN was grain size number and N_L was number of grain intercept.

$$GSN = 6.6439\, log_{10} N_L - 3.2877 \qquad (4)$$

Tensile and micro-vickers hardness test were used to confirm the effect of intercritical annealing on the mechanical properties. A tensile test was conducted at room temperature using the Tinnius Olsen 30 SL/Super L60 machine with a 25 mm/min cross-head speed. The specimens were prepared using wire cutting to obtain the dimension of sample sizes as shown in Fig. 2, according to ASTM E8/E8M-13a. While, the hardness test was carried out using the Mitutoyo HM 200 test equipment with a load of 1N and a loading time of 12 seconds. The hardness value was averaged from six position result.

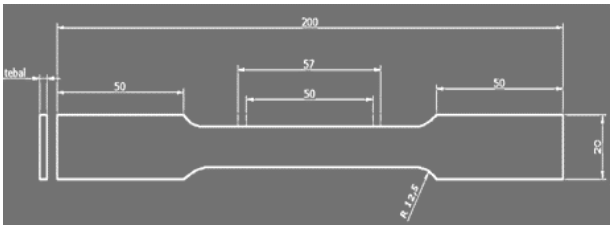

Figure 2. Dimension of tensile test carbon steel specimen

In the tensile test, the relationship between stress and strain is formulated as:

$$E = \sigma/\varepsilon \qquad (5)$$

Where E is the modulus of elasticity, σ is stress (MPa), and ε is strain (%). The strain hardening coefficient exponent (*n*) is a quantity that indicates the magnitude of the increase in strength and hardness due to plastic deformation.

The value of n flat metal specimens such as sheets or strips can be calculated from the force and extension data from the tensile test results of ASTM E8 / E8M -13a, using the general equation of flow stress σ with strain rate sensitivity (ASTM E 646), followed as Eq. 6.

$$\sigma = K.\varepsilon^{n} \qquad (6)$$

K is a material constant or strength coefficient [12]-[14]. Equation 5 has been corrected through a semi-logarithmic relationship [12]-[15].

3. Result and Discussion

3.1 Heat Treatment

Before experimenting, the TTT (time-temperature-transformation) and CCT (continuous cooling transformation) diagrams were simulated using JmatPro software to predict the microstructure evolution of the austenite phase after the austenitization process at 920 °C, depicted in Figure 3.

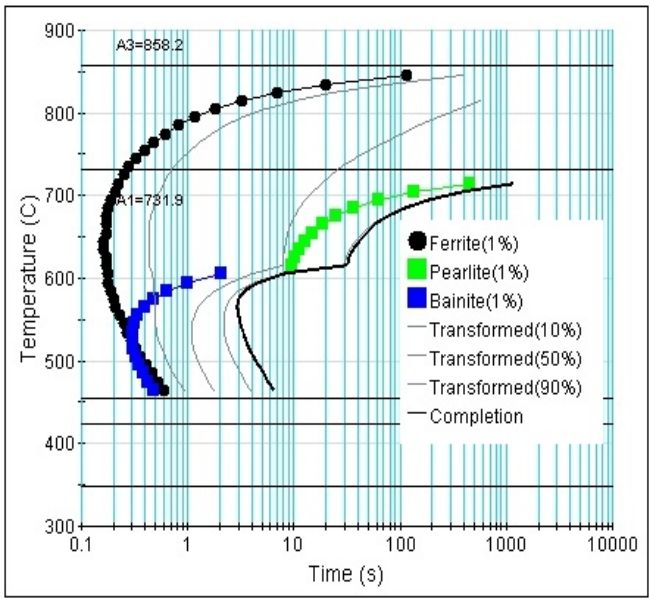

Figure 3. TTT diagram of tested steel

The intercritical zone was estimated at 731.9-858.2 °C, and the martensite was initially formed at 455 °C. Based on Figure 3, the time required for martensite formation is less than 1 minute, suggesting the cooling rate is very fast. Unfortunately, the ferrite also formed when the cooling time reached up to 0.2 s and was completed at 10-1000 s, concluding that slow cooling was required. In comparison, the pearlite transformation (green line) starts forming slower (10-1000s). According to the theory, the primary pearlite nucleation sites occurred at grain boundaries, causing the grain size of the austenite to increase as the austenitization temperature increases [15]. This cooling time from austenitization temperature to room temperature corresponds to the final phase formation after employing different cooling media.

3.2 Microstructure Analysis

Based on Figure 4(a), the as-received microstructure of tested steel consists of a ferrite

phase12 (light area) and pearlite (black area) with a 9.199-GSN (grain size number) equivalent to 13.23 μm [10].

received sample. It is concluded that the grain size depends on the cooling rate. The full martensite was formed when water quench was

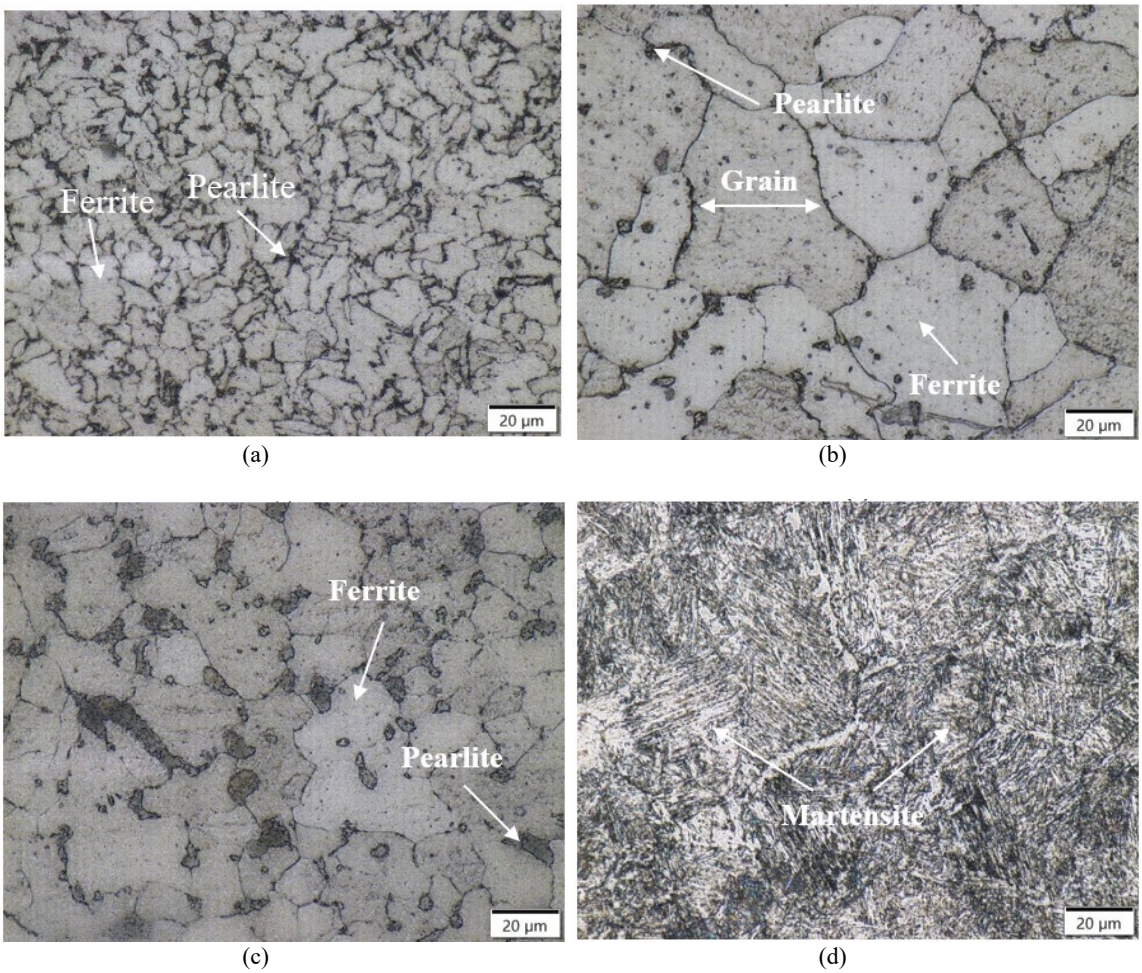

Figure 4. Microstructure of low carbon steel (a) as-received and after austenitizing at 920 °C with (b) furnace cooling, (c) air cooling, and (d) water quench

The microstructure evolution during the austenitization process at 920 ℃ for 30 minutes and subsequently cooled in different media is shown in Figures 4(b)-4(d). The cooling media used is furnace cooling, open-air cooling, and water cooling, which is used to generate different structures before intercritical anneal.

By heating at 920 ℃ for 30 minutes, the ferrite and pearlite transformed into an austenite phase. A significant phase transformation did not take place by furnace cooling (Fig. 4(b)), and only grain coarsening occurs to 6.2147 GSN (37.25 μm). The volume fraction of ferrite and pearlite is 82.81% and 17.19%, respectively. The open-air cooling does not trigger the phase transformation; therefore, the final phase remains ferrite (71.95%) and pearlite (29.05%) (Fig. 4(c)). After the air cooling process, the grain size (27.74 μm) is smaller than those processed by furnace cooling but still larger than the as-applied after austenitization (Fig. 4(d)). This result is in good agreement with the TTT diagram (Fig. 3), which was obtained by JMatPro software.

After getting the different initial structure, the intercritical annealed process was carried out at a temperature of 750 °C for 10 minutes, followed by quenching water. Figure 6 depicts the DP microstructures after intercritical annealed at 750 ℃, which transformed from the corresponding microstructure in Fig. 5. The dual-phase structure was obtained in all samples. In the furnace cooling + intercritical annealed sample, the smaller grain of the martensite phase can be seen with 18.36 vol.% in the grain boundary of ferrite (Fig. 5(a)). By heating in intercritical zone, the austenite was nucleated at the ferrite-pearlite interface and grew later until the pearlite transformation was completed. Because austenite nucleation is competitive in

recrystallized ferrite grains, it favors generating austenite networks, which subsequently transform into martensite networks during the quenching process [15]. Conversely, air cooling produces more martensite (27.85%) with nearly uniform distribution and coarsen martensite than furnace cooling. The average grain size is 38.82 μm and 31.02 μm for furnaces and open-air cooling, respectively. This difference is attributed to the initial structure before intercritical annealing (Figs. 4(b)-4(c)), which has a more uniform amount of pearlite that transforms into austenite when it passes through the A_{C1} line [5]-[6].

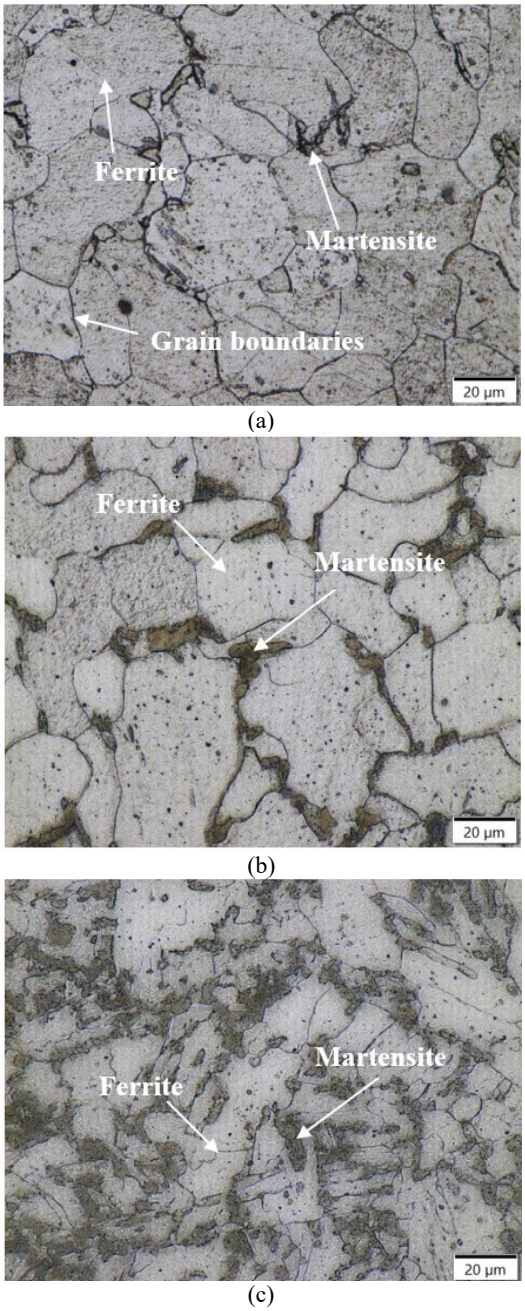

Figure 5. Microstructure after intercritical annealed with prior structure processed by (a) furnace cooling, (b) air cooling, and (c) water cooling

The intercritical annealing of the initial martensite structure produced by water quenching after austenitization generated a finer martensite than the other process (Fig. 5(c)). The amount of final martensite is higher (39.25%), and the average grain size is smaller (21.975 μm) of material water cooling + IA. When a prior-quenched structure is subjected to intercritical annealing, the martensite as a metastable phase has a driving energy to revert to its stable form and nucleate the austenite and fresh ferrite along the prior martensite boundary [1]. Furthermore, rapid cooling will transform the newly austenite into fresh martensite. It can be concluded that the phenomena are similar to the martemper process, which occurs in the suppression of carbide deposition and leads to the ferrite and martensite as the final structure [12].

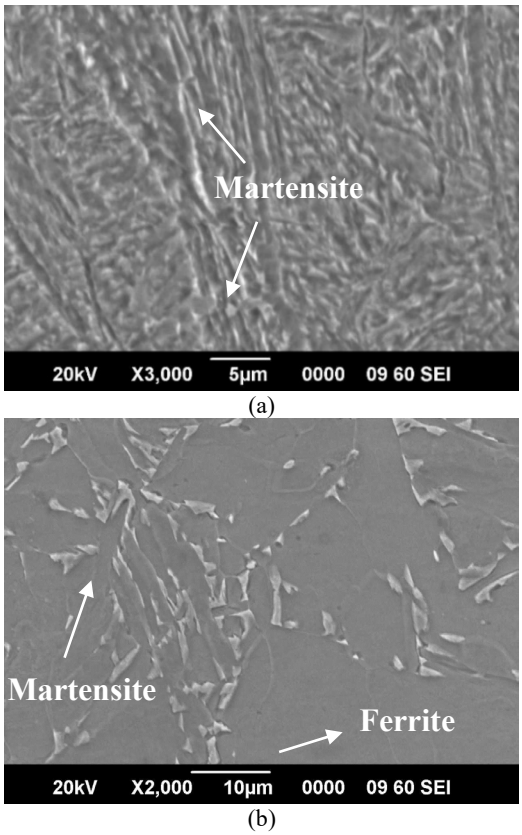

Figure 6. SEM image of quenched structure (a) before and (b) after intercritical annealed

The SEM (scanning electron microscope) image regarding the martensite structure before and after IA resulting from water quenching is shown in Figure 6. The full martensite after water quenching is visible with higher density (Fig. 6(a)) than after the intercritical annealing (Fig. 6(b)).

These results agree with the optical image, which shows another phase as ferrite after intercritical annealing. The fresh martensite is significantly smaller and shorter, less than 10μm.

More details of all the values of GSN, grain diameter, and phase fraction present in tested steel before and after the intercritical annealing process are presented in Table 3.

Table 3. Value of GSN, grain diameter, and phase fraction of tested steel before and after intercritical annealing

Code	GSN	Grain ⌀ (µm)	Phase Fraction (%)		
			Ferrite	Pearlite	Martensite
As-received	9.20	13.23	75.70	24.30	---
Furnace cooling	6.21	37.25	82.81	17.19	---
Open air cooling	7.31	27.74	70.95	29.05	---
Water cooling	---	12.27	---	---	100
Furnace cooling+IA	6.09	38.82	81.64	---	18.36
Open air cooling+IA	6.74	31.02	72.15	---	27.85
Water cooling+IA	7.74	21.97	60.75	---	39.25

3.3 Tensile Analysis

All specimens were subjected to a tensile test to confirm the stress-strain behavior under the applied tensile force, as shown in Figs. 7-8.

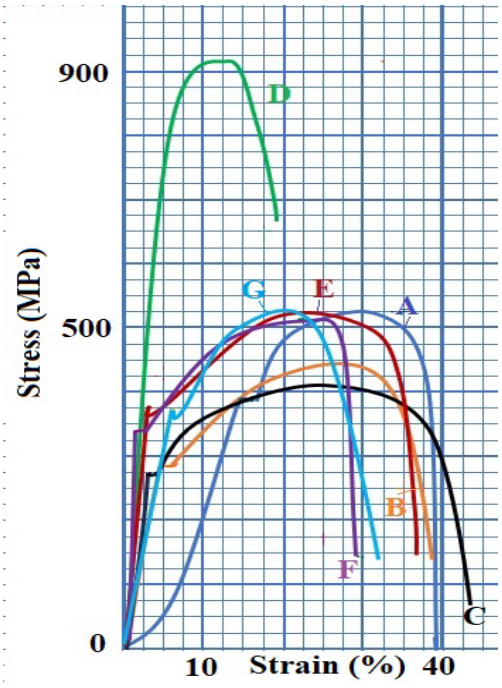

Figure 7. Tensile test results in tested steel (A = as-received; B = open-air cooling; C = Furnace cooling; D =. water cooling; E =. open air cooling+IA; F = furnace cooling + IA; G.= water cooling +IA)

Based on Figures 7-8, the as-received sample, consisting of a ferrite-pearlite structure, has 519 MPa of tensile strength and 39.2% elongation. The tensile properties after austenization vary depending on the cooling media. The tensile and yield strength increased as the cooling rate increased, considering grain size refinement followed the Hall-Petch relationship [16]. The UTS/YS (ultimate tensile strength yield strength) ratio decreased with the rising cooling rate up to 1.08. Rapid cooling in water medium obtained the highest tensile strength, ~919 MPa. Conversely, increasing tensile strength (Fig. 8(a)) is followed by decreasing elongation to 16.6% (Fig. 8(b)) as a consequence of complete martensite formation. Rapid cooling rates didn't give time for carbon diffusion into BCC (body-centered cubic) crystal, so the BCT (body-centered tetragonal) with high atomic packing density was formed during transformation. In addition, cooling in the furnace occurs more slowly than in the open air. This causes the grains in the furnace cooling to be larger, which causes them to become more ductile. As mentioned in the previous research, DP (dual phase) steels' stress-strain depicts low yield strength, continuous yielding, and high strain hardening [1].

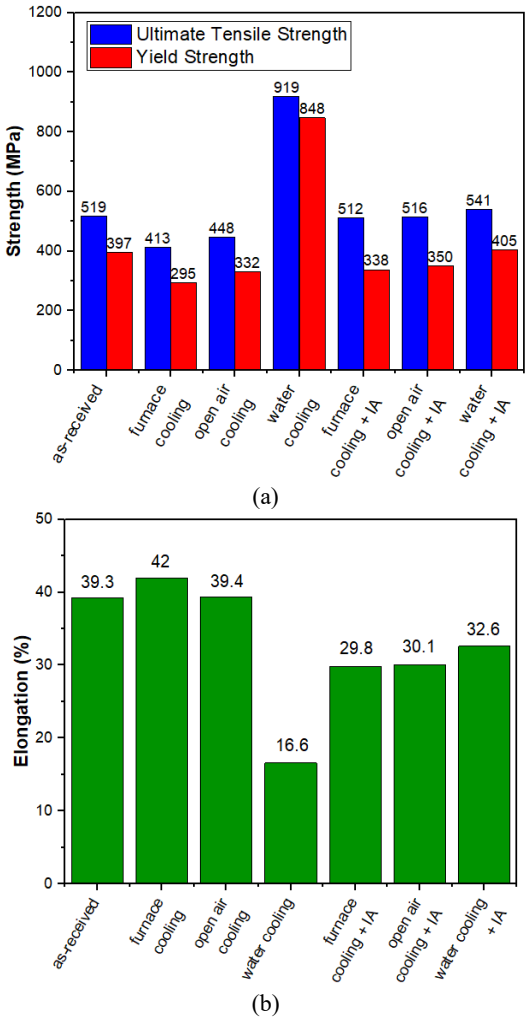

Figure 8. (a) Ultimate tensile and yield strength (b) elongation on low carbon steel before and after heat treatment + IA processing

Additionally, the dual-phase structure shows elongation maintenance around 29.8-32.6%,

although it has a brittle martensite structure (Fig 8(b)). As the cooling rate before the intercritical process increases, the tensile strength elongation improves up to 541 MPa, corresponding to the increased volume fraction of martensite (~39.25 vol.%, see Fig. 5(c)). Due to the shear and volume changes between austenite and martensite, it is expected that some unpinned dislocation in the surrounding of prior ferrite occurred and prevented yielding phenomenon, lead to a higher tensile strength [17]. Besides that, the different volume fractions and sizes of martensite in DP structures are also related to the strength and elongation of DP. More martensite volume fraction with uniform distribution as ferrite network provides higher UTS x ε properties.

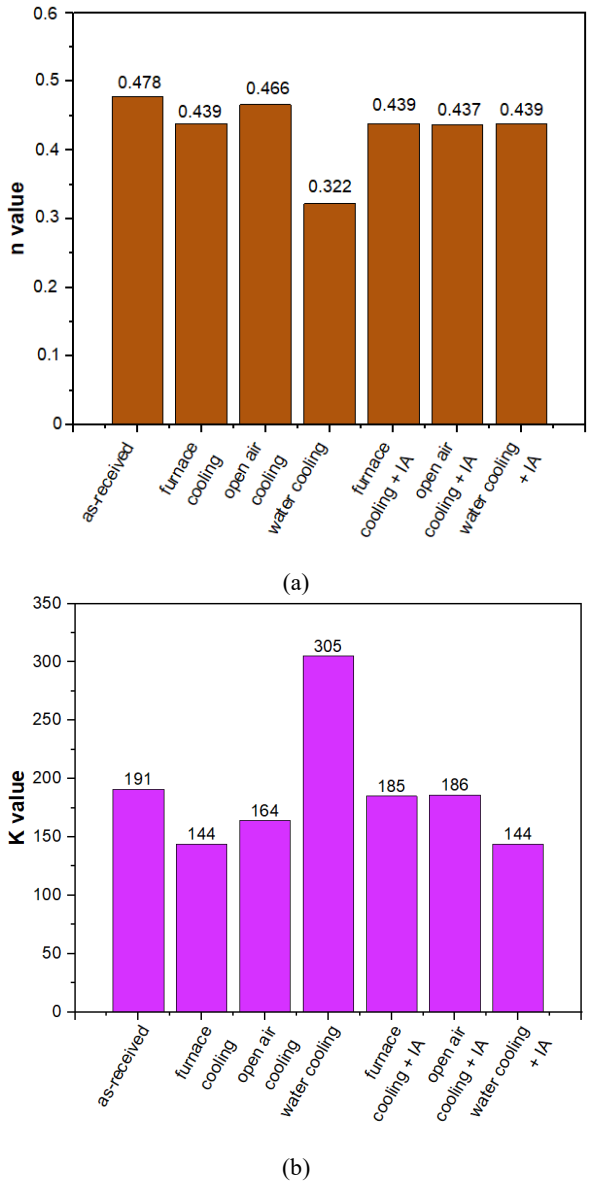

Figure 9. Tensile test results (a) n value and (b) K value in carbon steel before and after HT and IA processes

The strain hardening corresponding to the tensile curve is shown in Figure 9, represented by the work hardening exponent (n) and K values (Eq. 5).

The high strain hardening value indicates the possibility of deforming before instability and stretch before necking starts [1],[18]. For the ferritic-pearlite steel, the as-received steel has an the n value of 0.478 and the K value of 191.22. After austenitized at 920 °C, n value becomes lower, and K value becomes higher, resulting in the increasing cooling rate.

At the fully brittle martensite phase, the n value was lower (0.322) than the others, indicating the most insufficient work hardening due to the small area for plastic deformation. The strain hardening exponent slightly decreased around 0.437-0.439 after intercritical annealing, suggesting the dual-phase structure (ferrite + martensite) provides a similar behavior with other (ferrite+pearlite phase as a result of the furnace and open-air cooling). The work hardening rate of ferrite+martensite structure consists of three stages: (1) the initial gradient of ferrite glide was caused by moving dislocation, (2) the normal ferrite work hardening and constrained by martensite, and (3) co-deformation of both hardened ferrite and martensite [6],[15]. Zhao et al., [19] reported that the higher strain hardening occurred at initial plastic deformation due to the initial high density of free dislocation and the multiplication of dislocation in further strain. Nevertheless, the restraining ferrite deformation by martensite caused the decreasing strain hardening value. The work hardening rate of DP steels can be related to the function of volume fraction and particle size of martensite [17].

The prior water-quenched structure provide a higher strain hardening value of ~0.439, indicating the higher strain hardening ability of martensite tempered. This can be attributed to the uniform distribution of network martensite surrounding ferrite grain and fine grain of martensite (Figs. 5(c) and 6(b)), similar to Deng et al., result [16].

3.4 Hardness Test

The complete results of the hardness test with the Vickers method are shown in Figure 10. The results of the as-received material hardness test were 180 HV, whereas, after processing in the furnace and air, there was a decrease, namely 158 and 168 HV. This was due to the increase in grain size, making it softer. The quenching result in water shows an increase with a high hardness value, namely 347 HV. This indicates that the material becomes hard due to the dominance of the martensite phase.

The intercritical annealing increased in the material's hardness compared to the as-received state, namely 183 and 186, and 199 Hv for the specimens cooled in the furnace, air, and water, respectively.

Because the initial structure persists in ferrite and pearlite before intercritical annealing, the hardness due to the furnace and open-air cooling is lower than that of water cooling. The full martensite as the initial structure provided a high martensite volume fraction of ~ 39.25% after intercritical annealing. When heated again in the intercritical annealing zone, some of the martensite phase returns to the ferrite, although there is still martensite left and new martensite is formed. The martensite transformation induced by intercritical annealing caused a decrease in hardness (from 347 HV to 199 HV).

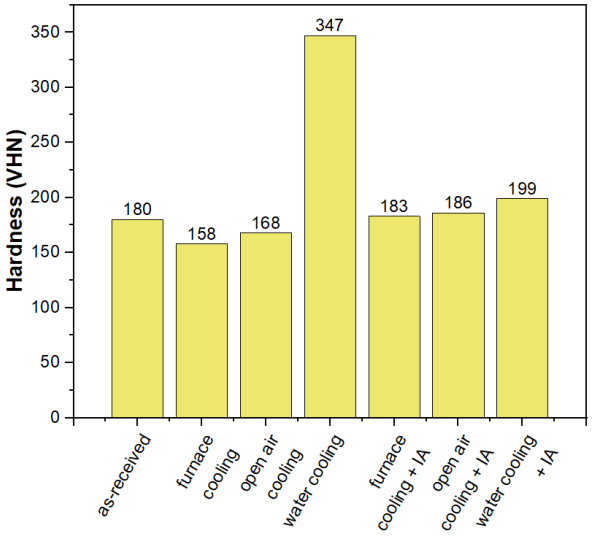

Figure 10. Vickers hardness test results of tested steel

4. CONCLUSION

In this work, the different cooling rates from austenitization lead to the other initial structures of low-alloy carbon steel before intercritical annealing. The other initial structures, in turn, resulted in dual-phase steel with different microstructure and mechanical properties following the intercritical annealing. The slower cooling (with furnace and open-air cooling) provides the pearlite + ferrite as the initial structure, whereas the rapid cooling generates the martensite structure. As the cooling rate increased, the tensile strength increased to ~919 MPa, and the elongation decreased to ~16.6%. During intercritical annealing, the pearlite was transformed into austenite after passing the AC1 temperature and led the austenite network near recrystallized ferrite with 38.817 μm of grain size. As the ferrite-martensite phase, the water-quenched structure provides the uniformly finer martensite of less than 10 μm, correlating the higher tensile strength (541 MPa), more elongation (32.6%), and higher hardness (199 VHN). Nevertheless, the differences in initial structure have an insignificant effect on strain-hardening behavior.

ACKNOWLEDGMENT

Thank you to the Metallurgical Research Center - National Research and Innovation Agency, which has funded this research.

REFERENCES

[1] M. Soliman and H. Palkowski, "Strain hardening dependence on the structure in dual-phase steels," *Steel Res. Int.*, vol. 92, no. 4, pp. 1-15, 2021. Doi: 10.1002/srin.202000518.

[2] J. Samei, Y. Salib, M. Amirmaleki, and D. S. Wilkinson, "The role of microstructure on edge cracks in dual phase and quench and partitioning steels subject to severe cold rolling," *Scr. Mater.*, vol. 173, pp. 86-90, 2019. Doi: 10.1016/j.scriptamat.2019.08.012.

[3] T. Yalçinkaya, S. O. Çakmak, and C. Tekoğlu, "A crystal plasticity based finite element framework for RVE calculations of two-phase materials: Void nucleation in dual-phase steels," *Finite Elem. Anal. Des.*, vol. 187, pp. 103510, 2021. Doi: 10.1016/j.finel.2020.103510.

[4] A. Kalhor, M. Soleimani, H. Mirzadeh, and V. Uthaisangsuk, "A review of recent progress in mechanical and corrosion properties of dual phase steels," *Arch. Civ. Mech. Eng.*, vol. 20, no. 3, pp. 1-14, 2020. Doi: 10.1007/s43452-020-00088-0.

[5] A. Kalhor and H. Mirzadeh, "Tailoring the microstructure and mechanical properties of dual phase steel based on the initial microstructure," *Steel Res. Int.*, vol. 88, no. 8, pp. 1-8, 2017. Doi: 10.1002/srin.201600385.

[6] F. Jamei, H. Mirzadeh, and M. Zamani, "Synergistic effects of holding time at intercritical annealing temperature and initial microstructure on the mechanical properties of dual phase steel," *Mater. Sci. Eng. A*, vol. 750, pp. 125-131, 2019. Doi: 10.1016/j.msea.2019.02.052.

[7] J. Adamczyk, and A.Grjcar "Heat treatment and mechanical properties of low-carbon steel with dual-phase

microstructure," *Journal of Achievement in Materials and Manufacturing Engineering,* vol. 22, no. 1, 2007.

[8] H. Dannoshita, T. Ogawa, K. Maruoka, and K. Ushioda, "Effect of initial microstructures on austenite formation behavior during intercritical annealing in low-carbon steel," *Mater. Trans.*, vol. 60, no. 1, pp. 165-168, 2019. Doi: 10.2320/matertrans.M2018298.

[9] M. Maleki, H. Mirzadeh, and M. Zamani, "Effect of intercritical annealing time at pearlite dissolution finish temperature (Ac1f) on mechanical properties of low-carbon dual-phase steel," *J. Mater. Eng. Perform.*, vol. 28, no. 4, pp. 2178-2183, 2019. Doi: 10.1007/s11665-019-04009-y.

[10] M. Maleki, H. Mirzadeh, and M. Zamani, "Effect of intercritical annealing on mechanical properties and work-hardening response of high formability dual phase steel," *Steel Res. Int.*, vol. 89, no. 4, pp. 1-7, 2018. Doi: 10.1002/srin.201700412.

[11] ASTM International, "Standard test methods for determining average grain size," E 112-12, 2010. Doi: 10.1520/E0112-12.1.4.

[12] J. Adamczyk and A. Grajcar, "Heat treatment and mechanical properties of low-carbon steel with dual-phase microstructure manufacturing and processing," *J. Achiev. Mater. Manuf. Eng.*, vol. 22, no. 1, pp. 13-20, 2007.

[13] N. Lanzillotto and F. B. Pickering, "Structure-property dual-phase steels relationships in," *Met. Sci.*, vol. 16, no. August, pp. 371-382, 1982.

[14] M. A. M. Gurgel, E. S. B. Junior, R. S. Teixeira, G. O. Nascimento, S. S. Oliveira, D. N. F. Leite, L. P. Moreira, L. P. Brandao, and A. S. Paula , "Microstructure and continuous cooling transformation of an Fe-7.1Al-0.7Mn-0.4C-0.3Nb Alloy," *Metals (Basel).*, vol. 12, no. 8, pp. 1-16, 2022. Doi: 10.3390/met12081305.

[15] P. D. Basoeki, "Effects of DP steel microstructure on the disappearance of discontinuous yielding," *MATEC Web Conf.*, vol. 204, pp. 1-8, 2018. Doi: 10.1051/matecconf/201820407013.

[16] Y. G. Deng, H. S. Di, and R. D. K. Misra, "On significance of initial microstructure in governing mechanical behavior and fracture of dual-phase steels," *J. Iron Steel Res. Int.*, vol. 25, no. 9, pp. 932-942, 2018. Doi: 10.1007/s42243-018-0133-0.

[17] H. Mirzadeh, M. Alibeyki, and M. Najafi, "Unraveling the initial microstructure effects on mechanical properties and work-hardening capacity of dual-phase steel," *Metall. Mater. Trans. A Phys. Metall. Mater. Sci.*, vol. 48, no. 10, pp. 4565-4573, 2017. Doi: 10.1007/s11661-017-4246-z.

[18] Y. Mazaheri, A. Kermanpur, and A. Najafizadeh, "A novel route for development of ultrahigh strength dual phase steels," *Mater. Sci. Eng. A*, vol. 619, pp. 1-11, 2014. Doi: 10.1016/j.msea.2014.09.058.

[19] Z. Zhao, T. Tong, J. Liang, H. Yin, A. Zhao, and D. Tang, "Microstructure, mechanical properties and fracture behavior of ultra-high strength dual-phase steel," *Mater. Sci. Eng. A*, vol. 618, pp. 182-188, 2014. Doi: 10.1016/j.msea.2014.09.005.

AUTHOR INDEX

SUBJECT INDEX